## REVIEW

Check for updates

# Advanced inorganic nanomaterials for high-performance electrochromic applications

Zekun Huang,†[a,b] Liping Feng,†[b] Xianjie Xia,†[b] Jing Zhao,[b] Penglu Qi,[b] Yiting Wang,[b] Junhua Zhou,[b] Laifa Shen, [ID] [a,b] Shengliang Zhang [ID] *[a,b] and Xiaogang Zhang [ID] *[a,b]

Electrochromic materials and devices with the capability of dynamic optical regulation have attracted considerable attention recently and have shown a variety of potential applications including energy-efficient smart windows, multicolor displays, atuto-diming mirrors, military camouflage, and adaptive thermal management due to the advantages of active control, wide wavelength modulation, and low energy consumption. However, its development still experiences a number of issues such as long response time and inadequate durability. Nanostructuring has demonstrated that it is an effective strategy to improve the electrochromic performance of the materials due to the increased reaction active sites and the reduced ion diffusion distance. Various advanced inorganic nanomaterials with high electrochromic performance have been developed recently, significantly contributing to the development of electrochromic applications. In this review, we systematically introduce and discuss the recent advances in advanced inorganic nanomaterials including zero-, one-, and two-dimensional materials for high-performance electrochromic applications. Finally, we outline the current major challenges and our perspectives for the future development of nanostructured electrochromic materials and applications.

[a]*State Key Laboratory of Mechanics and Control for Aerospace Structures, Nanjing University of Aeronautics and Astronautics, No. 29 Yudao Street, Nanjing 210016, China. E-mail: zhangsl@nuaa.edu.cn, azhangxg@nuaa.edu.cn*
[b]*Jiangsu Key Laboratory of Electrochemical Energy Storage Technologies, College of Materials Science and Technology, Nanjing University of Aeronautics and Astronautics, Nanjing 210016, China*
†These authors contributed equally.

*Shengliang Zhang is Associate Professor at the College of Materials Science and Technology, Nanjing University of Aeronautics and Astronautics. He received his Ph.D. degree from the National University of Singapore in 2019. He then started his postdoctoral research at the National University of Singapore between 2019 and 2020. His current research interests include electrochromic materials and devices, multispectral adaptive camouflage, and intelligent photothermal regulation.*

**Shengliang Zhang**

## 1. Introduction

Electrochromism is the phenomenon where optical properties (transmittance, absorbance, reflectance, or emittance) of a material are dynamically and reversibly changed by the application of a small external electric field.[1,2] This preeminent technology has shown a variety of potential applications including energy-efficient smart windows,[3–10] multicolor displays,[11–13] atuto-diming mirrors, military camouflage,[14–16] and adaptive thermal management[17–19] (Fig. 1) due to the advantages of active control, wide wavelength modulation, and low energy consumption. Therefore, electrochromic (EC) materials and devices have attracted increasing attention from scientific and industrial communities and have become a hot research topic in recent years.

An EC device typically comprises an EC layer on a conductive electrode, an electrolyte layer, and an ion storage layer on a conductive electrode.[1,2] The mechanism of electrochromism can be attributed to the ions and electrons that are injected/extracted into/from the EC materials under an applied voltage, resulting in the redox reaction of materials and reversible changes in optical properties.[20–24] The optical modulation, switching time, coloration efficiency, bistability, cycling stability, and energy consumption are the main evaluating parameters of EC materials and devices.

For an EC device, the EC materials are undoubtedly the core components, playing the key function of dynamically tuning the optical properties. Generally, EC materials can be
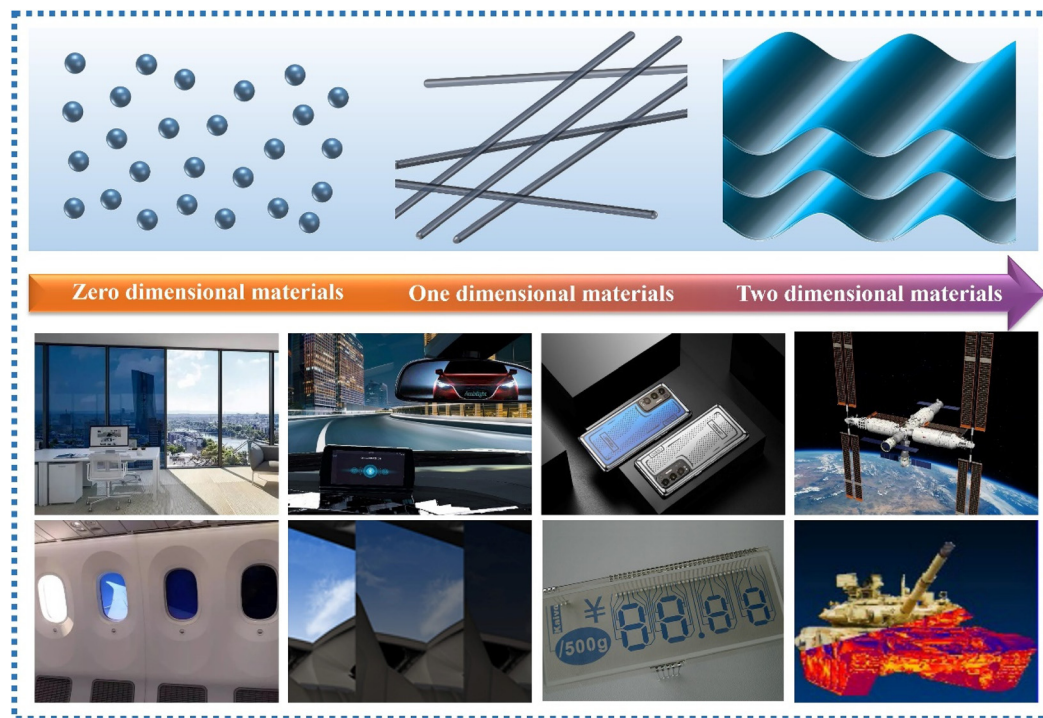
**Fig. 1** Schematic diagram of inorganic electrochromic nanomaterials and their promising applications.

divided into organic materials and inorganic materials.[20–22] Organic EC materials mainly include organic small molecules (viologen and its derivatives)[25] and conducting polymers (*e.g.*, polyaniline, polythiophene, polypyrrole, and their derivatives).[17,26–28] The organic EC materials stand out due to their multicolor tunability, fast response, flexibility, structural modifiability, and easy processing, which endow them wide potential applications, especially in displays and wearable devices. Recently, inorganic EC materials have also been widely investigated because of their excellent stability, wide range of working temperature, and wide spectral modulation.[29–31] Transition metal oxides[32–36] (*e.g.*, $WO_3$, $MoO_3$, $TiO_2$, $NiO$, and $V_2O_5$), Prussian blue (PB),[37,38] and carbon materials[18,19] are typical inorganic EC materials. Due to the high optical modulation and high stability against high temperature and strong light, inorganic EC materials have been suggested as the most suitable materials for smart windows and thermal management in some extreme application environments.

Although inorganic EC materials have shown a number of advantages, the slow switching speed is the major issue and hinders their practical applications. Based on the mechanism of electrochromism, the response time is related with the ion diffusion kinetics and ion diffusion distance in electrochromic materials. Nanostructuring is therefore an effective strategy to improve the switching speed of the materials due to the increased ion diffusion speed and the reduced ion diffusion distance.[29–31] In addition, nanomaterials usually have a high surface area, which could accommodate more ions and then increase the optical modulation. Moreover, nanostructuring can also alleviate the volume expansion during ion intercala-

tion and reduce the possibility of ion-trapping in EC materials, which is clearly beneficial for enhancing the cycling stability. Consequently, lots of advanced inorganic nanomaterials with high electrochromic performance have been developed, especially in the last 5 years,[39–47] which notably contributes to the development of electrochromic applications.

Although a few literature reviews on electrochromic materials and devices have been reported,[29–31] there is a strong demand for a timely and updated comprehensive overview of recent progress (especially in the near 3 years) on advanced inorganic nanomaterials for high-performance electrochromic applications. In this review, we systematically introduce and discuss the recent advances in advanced inorganic electrochromic nanomaterials including zero dimensional (0D) materials (nanoparticles and quantum dots), one dimensional (1D) materials (nanowires and nanorods), and two dimensional (2D) materials. Finally, we outline the current major challenges and our perspectives for the future development of nanostructured inorganic electrochromic materials and applications. We hope that this review provides readers with a systematic perspective on advanced inorganic electrochromic nanomaterials, promoting the development of electrochromic fields.

## 2. Inorganic nanomaterials for EC devices

### 2.1. Zero dimensional (0D) inorganic EC materials

Zero dimensional (0D) nanomaterials mainly refer to nanoparticles and quantum dots, which are at the nanometer level

in all three dimensions. Therefore, 0D nanomaterials can notably reduce the ion diffusion distance and increase the ion diffusion speed and ion storage sites, significantly improving the EC performance of inorganic materials. In the following content, we mainly introduce and discuss the recent progress on 0D transition metal oxides.

**2.1.1. 0D tungsten oxides.** Tungsten oxide ($WO_x$), as a classic inorganic EC material, has been extensively studied due to its excellent performance and wide range of applications. Milliron *et al.* prepared $WO_{3-x}$ nanoparticles (Fig. 2a) by the colloidal method and used them as the near-infrared (NIR) selective electrochromic material for building the dual-band nanocomposites ($WO_{3-x}$-$NbO_x$, Fig. 2b).[36] Due to the nanostructure and strong localized surface plasmon resonance

(LSPR) of $WO_{3-x}$ nanoparticles, the prepared nanocomposites exhibited the enhanced dual-band electrochromic performance with efficient independent control of visible (VIS) light and NIR (Fig. 2c). The optical modulation and switching speed were also improved due to the large surface area and fast ion diffusion coefficient.

Doping is an efficient method to improve the performance and adjust the nanostructures of $WO_3$. Recently, Cao *et al.* reported a porous Ti-doped $WO_3$ nanoparticle film (Fig. 2d) prepared by the facile sol–gel method with polyvinylpyrrolidone (PVP) as the foaming agent.[48] Because of the existence of $Ti^{4+}$ in the $WO_3$ host, it can change the crystalline phase of $WO_3$ from the monoclinic to cubic phase. It also can prevent repeated crystal transformation (monoclinic ↔ tetragonal ↔



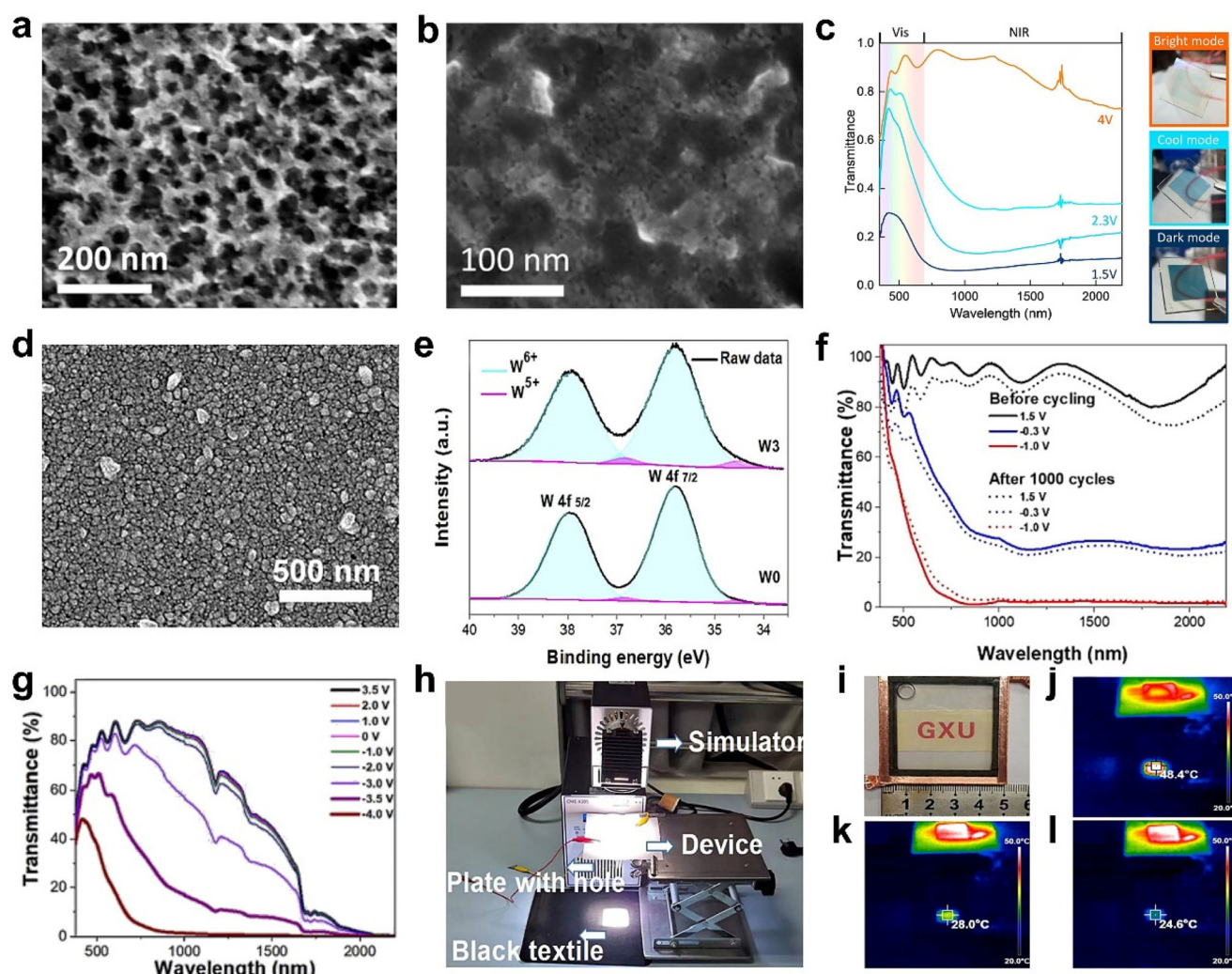**Fig. 2** (a) TEM image of $WO_{3-x}$ nanoparticles. (b) SEM image of $WO_{3-x}$-$NbO_x$ nanocomposite. (c) Transmittance spectra of the $WO_{3-x}$-$NbO_x$ composite film at different applied potentials and the corresponding photos of the sample. (a–c) Adapted with permission from ref. 36. Copyright 2015, American Chemical Society. (d) SEM image of the Ti-$WO_3$ film. (e) XPS spectra of W 4f. (f) Optical transmittance spectra of the Ti-$WO_3$ film before and after 1000 cycles. (g) Optical transmittance of the assembled device at different voltages. (h) Simulation of sunshine in the home-built test system. (i) Digital photo of the device under natural light. Infrared thermography images and temperature of the device in the bright (j), cool (k), and dark (l) modes after the AM 1.5 sunlight simulator is irradiated for the same time. (d–l) Adapted with permission from ref. 48. Copyright 2022, Elsevier.

cubic) and decrease the number of Li$^+$ traps. Therefore, the Ti-WO$_3$ film exhibited better cyclic stability than the WO$_3$ film. Furthermore, the introduction of foaming agent PVP polymer during the film preparation was able to alter the nanostructure of the Ti-WO$_3$ film and increase the active surface and the oxygen vacancy concentration (Fig. 2e). The optimal Ti-WO$_3$ film showed excellent dual-band electrochromic properties (Fig. 2f), including high optical modulation (84.9% at 633 nm and 90.3% at 1200 nm), high coloration efficiency, and quick switching speed. The Ti-WO$_3$ films also realized the independent control of VIS light and NIR, which can be attributed to the tunable LSPR induced by oxygen vacancies. In addition, a demonstrative device (5 × 5 cm$^2$) also showed good dual-band electrochromic performance as the film (Fig. 2g) and also displayed effective management of heat and light of sunlight (Fig. 2h–l).

Beside WO$_3$ nanoparticles, WO$_3$ quantum dots (QDs) with smaller size were also investigated for EC applications. Zhao et al.[49] reported nonstoichiometric WO$_{3−x}$ QDs (Fig. 3a) with a small size of ~1.6 nm and large surface-to-volume ratio, which significantly shortened the ions diffusion paths and increased the contact area between electrode materials with electrolyte/collector. Therefore, the WO$_{3−x}$ QDs realized a large optical modulation and an extremely fast switching speed of 0.9/1.0 s (Fig. 3b and c). Although conductive pyridine wrapped on the surface of WO$_3$ QDs could provide the fast reaction rate, the water solubility of pyridine and the strong corrosiveness of hydrogen ion aqueous electrolytes cause the poor cycle stability. Recently, Gao et al. demonstrated WO$_3$ QDs (~1.2 nm) without organic overlayer obtained through the dialysis process (Fig. 3d).[50] The WO$_3$ QD film was prepared by atmospheric pressure solution-based deposition (APSD) without any post-treatment, which exhibited excellent EC performance with either Li$^+$ or Al$^{3+}$ electrolytes: a large optical contrast (97.8% and 94.1% at 633 nm), a fast switching speed (4.5 s and 13.5 s for coloring, 4 s and 10 s for bleaching), and an ultralong cycle life (10 000 cycles with 10% optical contrast loss and 20 000 cycles without degeneration at 633 nm). Among them, Al$^{3+}$ with a smaller ion radius (0.53 Å) than Li$^+$ (0.76 Å) are beneficial for the ion insertion/extraction, resulting in smaller volume expansion of the host framework and improving the EC performance (Fig. 3e and f). Compared to traditional film-making methods, inkjet printing multifunctional technology is a potential candidate method, which can not only achieve large-scale customized pattern printing but also significantly reduce material waste.[51–53] But most printing inks require a number of additives to regulate the rheological properties of the ink and the uniformity of the pattern.[54] Additives need to be removed through high-temperature annealing, which not only introduces the complexity of synthesis but may also cause degradation of most flexible substrates. Recently, Fan et al. reported WO$_3$ nanocrystal (NC) inks based on ethanol (EtOH), isopropanol (IPA), N-methyl-2-pyrrolidone (NMP), and dimethylformamide (DMF) as solvent without any additives.[55] The high-quality concentrated ink with small size WO$_{3−x}$ nanocrystals can realize uniform printing and effectively reduce the

materials waste and the printing cost. The printed WO$_{3−x}$ (Fig. 3g and h) exhibited a large optical modulation (76% at 633 nm), a high coloration efficiency (97.7 cm$^2$ C$^{−1}$), and fast switching response (3.7 s for bleaching, 4.5 s for coloring). Furthermore, a demonstrating device consisted of metallic zinc and the printed WO$_{3−x}$ electrode was assembled, which exhibited rechargeable capacitive energy, good cycle stability (70% of capacitance retention after 1000 cycles), and excellent flexibility (Fig. 3i–k).

**2.1.2. 0D titanium oxides.** Titanium oxide (TiO$_2$) with such desirable material features as chemical stability, environmental compatibility, low cost, and earth abundance is another promising candidate as active EC material, which consisted of [TiO$_6$] octahedrons, forming large vacant sites to bear ions.[31,56] The intercalation of guest ions will lead to the localization of implanted electrons on Ti cations, resulting in a decrease in visible light transmission.[57] Giannuzzi et al. reported that TiO$_2$ nanoparticles (~10 nm) was synthesized through a green aqueous sol–gel strategy.[58] The TiO$_2$ film exhibited better EC performance than commercial ones, including an optical modification of 63% at 550 nm and a superior cycling stability due to the enhanced pseudocapacitive contribution to ion storage. Although reducing particle size can improve the EC performance, pure titanium dioxide still has lower performance compared to other electrochromic materials. Encouragingly, TiO$_2$ can be doped with aliovalent atoms to enhance the LSPR and improve the EC performance, especially for NIR-selective modulation.[59] As early as 2013, Milliron et al. prepared Nb-doped TiO$_2$ through colloidal synthesis and found that the incorporation of Nb could lead to tune the LSPR from VIS light to mid-infrared.[59] Subsequently, Dahlman et al. prepared Nb-doped TiO$_2$-based dual band EC films, which could afford four EC modes including bright, cool, dark, and warm through capacitive charging and structural phase transition.[60]

Recently, Cao et al. prepared different metal-doped TiO$_2$ nanocrystals (Mo, W, and Nb-doped TiO$_2$) using a simple one pot method and discussed their LSPR absorption peaks (Fig. 4a and b).[61] With the increasing concentration of free carriers, the LSPR absorption peaks gradually blue shift. Although doping with aliovalent ions can improve the electrochemical performance of TiO$_2$ nanocrystals (NCs), the larger the mismatch between the doping ion radius and the Ti$^{4+}$ radius, the more difficult it is to doping due to the "self-purification" effect.[62] Cao et al. developed a fluoride-assisted synthesis of metal-doped TiO$_2$ NCs, which realized effective aliovalent doping and good uniformity control.[57] Meanwhile, Ta-doped TiO$_2$ NCs with an average particle size of ~11.6 nm were prepared for EC applications (Fig. 4c). The substitution of Ta$^{5+}$ on Ti$^{4+}$ sites generated of a lot of free carriers in the conduction band of the TiO$_2$ NCs to activate the LSPR effect. Consequently, the Ta-TiO$_2$ NCs films not only showed the independent control of VIS and NIR (Fig. 4e) but also exhibited a high optical modulation of 86.3% at 550 nm and 81.4% at 1600 nm and excellent cycling stability. They also prepared a dual-band EC energy storage device based on Ta-doped TiO$_2$
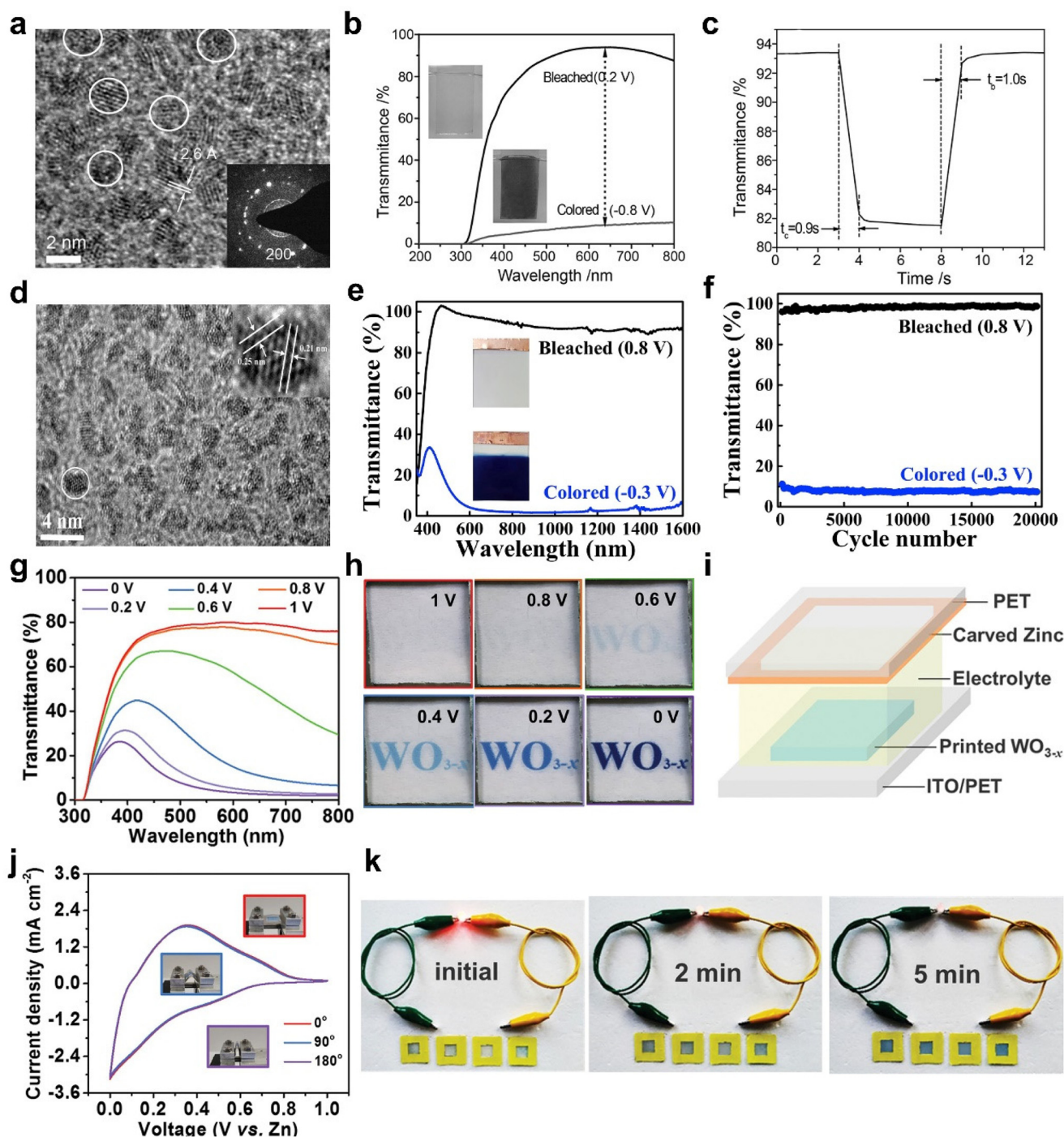
**Fig. 3** (a) High-resolution TEM image and selected area electron diffraction (SAED) pattern of $WO_{3-x}$ QDs. (b) Optical transmittance spectra and (c) switching speed of $WO_{3-x}$ QD films. (a–c) Adapted with permission from ref. 49. Copyright 2014, Wiley-VCH. (d) High-resolution TEM image of the as-prepared $WO_3$ QDs. (e) Optical transmittance spectra and (f) cycling performance of $WO_3$ QDs films in an $Al^{3+}$-based electrolyte. (d–f) Adapted with permission from ref. 50. Copyright 2020, Elsevier. Electrochemical characterizations of the inkjet-printed $WO_{3-x}$ film. (g) Transmittance spectra and (h) digital images of $WO_{3-x}$ films. (i) Configuration of the assembled device. (j) Cyclic voltammogram (CV) curves at 50 mV s$^{-1}$ under various bending conditions. (k) A LED is powered by electrochromic cells. (g–k) Adapted with permission from ref. 55. Copyright 2020, Wiley-VCh.

NCs, which exhibited good dual-band EC modulation and high energy storage performance (Fig. 4f–i).[41] This device provides a template for future multifunctional dual band electrochromic smart windows with energy storage function.

Recently, Cao *et al.* adopted the strategy of W doping to achieve the reversible intercalation/de-intercalation of $Zn^{2+}$ in $TiO_2$ NCs.[42] The prepared EC device (Fig. 4j–m) displayed high optical modulation (77.6% and 66% at 550 nm), fast response
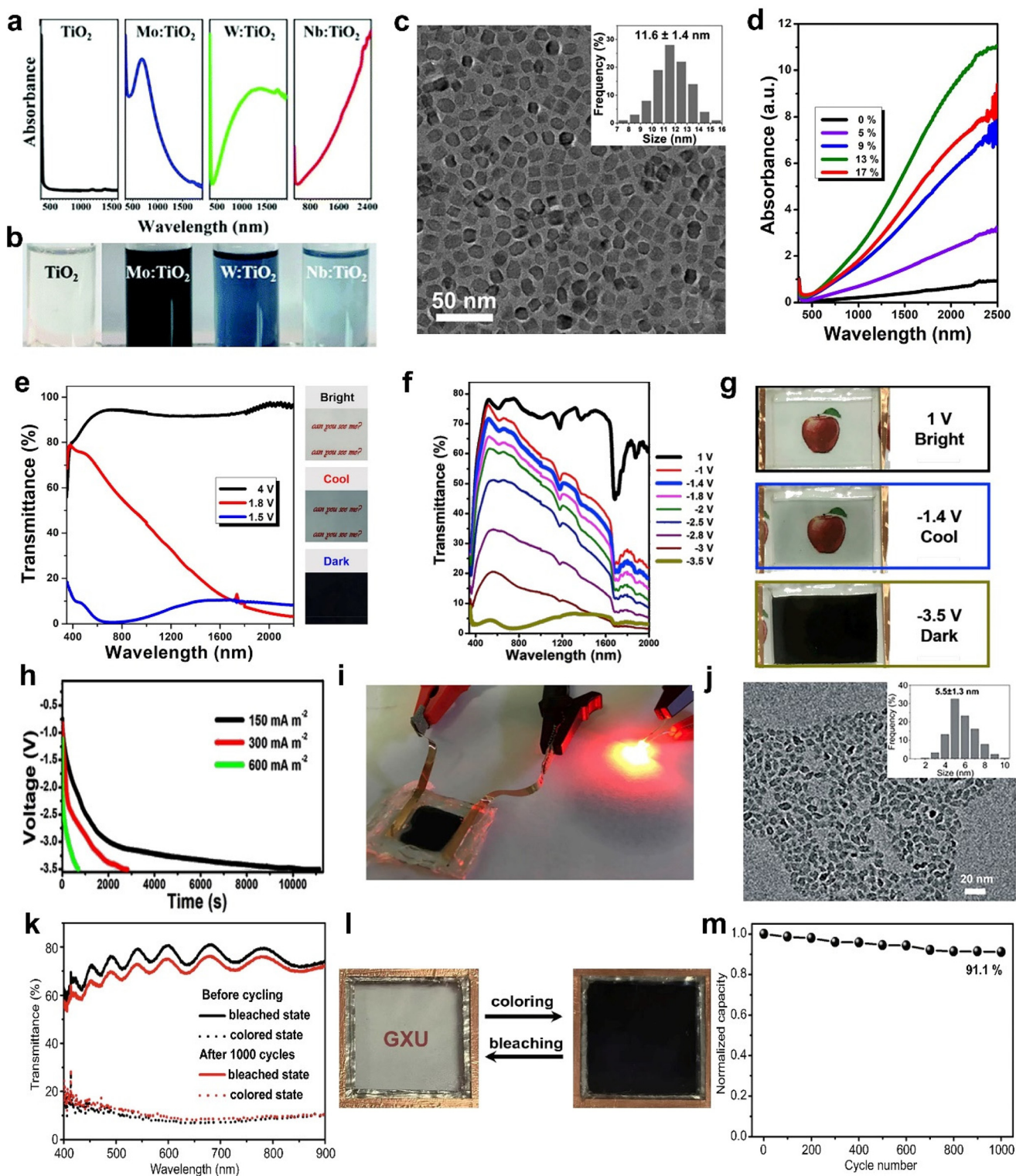
Fig. 4 (a) Absorption spectra and (b) digital photos of pristine $TiO_2$, Mo-$TiO_2$, W-$TiO_2$, and Nb-$TiO_2$ nanoparticles. (a and b) Adapted with permission from ref. 61. Copyright 2018, Royal Society of Chemistry. (c) TEM image and (d) normalized absorption spectra of Ta-doped $TiO_2$ nanoparticles. (e) Transmittance spectra and corresponding digital photos of a Ta-doped $TiO_2$ film. (c–e) Adapted with permission from ref. 57. Copyright 2018, American Chemical Society. (f) Optical transmittance spectra, (g) digital photos, (h) galvanostatic charging curves, and (i) powering a red LED of the device based on Ta-doped $TiO_2$. (f–i) Adapted with permission from ref. 41. Copyright 2018, Elsevier. (j) TEM image and size distributions (inset) of W-$TiO_2$. (k) Optical transmittance spectra, (l) photographs, and (m) cycling stability of the device. (j–m) Adapted with permission from ref. 42. Copyright 2021, Springer Nature.

time (9 s for coloring, 2.7 s for bleaching), and good cycling stability (8.2% optical modulation loss after 1000 cycles).[42]

Although aliovalent doping can enhance the performance of $TiO_2$, lattice strain and lattice distortion caused by the radius mismatch of dopant and $Ti^{4+}$ can have adverse effects on the stability of the host lattice structure and ion diffusion.[62] In addition to the method of aliovalent doping, oxygen-vacancy creation is also an effective method to improve the performance of $TiO_2$ NCs. The existence of oxygen vacancies would increase the free carrier concentration of $TiO_2$ NCs and reduce the energy barrier of $Li^+$ diffusion in $TiO_2$, realizing fast reaction speed.[63] Recently, Zhang et al. reported high-quality oxygen-deficient titanium dioxide ($TiO_{2-x}$) NCs synthesized by F-assisted colloidal method. The prepared $TiO_{2-x}$ NCs showed high uniformity and strong tunable LSPR performance (Fig. 5a).[64] The LSPR absorption intensity increased with the F to Ti ratio of the precursor mixture from 0 to 0.6 (Fig. 5b). Oxygen vacancies not only confer good NIR-selective modulation but also improve the $Li^+$ diffusion in the $TiO_{2-x}$ host, circumventing the disadvantage of aliovalent substitutional doping with ion diffusion. Consequently, the optimized $TiO_{2-x}$ NC films (Fig. 5c–g) are able to modulate the NIR and VIS light transmittance independently and effectively in three distinct modes with high optical modulation (95.5% and 90.5% at 633 and at 1200 nm, respectively), fast switching speed, high bist-ability, and a remarkable cycling stability (4.4% capacity loss after 2000 cycles). When a 3.5 V (vs. $Li^+/Li$) is applied to the electrode, the film achieves a "bright" mode, exhibiting high transmittance in the VIS and NIR. At a potential of 1.8 V, the $Li^+$ is adsorbed on the electrode surface and undergo LSPR absorption, resulting in blocking most of the NIR while maintaining a high VIS transmittance (the "cool" mode). In the "dark" mode at 1.5 V, the $Li^+$ intercalates into the titanium oxide host, simultaneously blocking VIS and NIR transmittance owing to the phase change from tetragonal anatase $TiO_2$ to orthorhombic $Li_xTiO_2$. Furthermore, an impressive dual-band electrochromic performance is also demonstrated in prototype devices (Fig. 5h and i). The use of $TiO_{2-x}$ NCs enables the assembled windows to recycle a large fraction of energy consumed in the coloration process to reduce the energy consumption in a round-trip electrochromic operation.

**2.1.3. 0D nickel oxides.** Nickel (Ni)-based EC materials, as classic electrochromic anode materials, have been broadly studied due to their low cost and neutral coloring feature.[65] Among them, nickel oxide (NiO) is identified as one of the most promising dark coloration electrochromic materials,
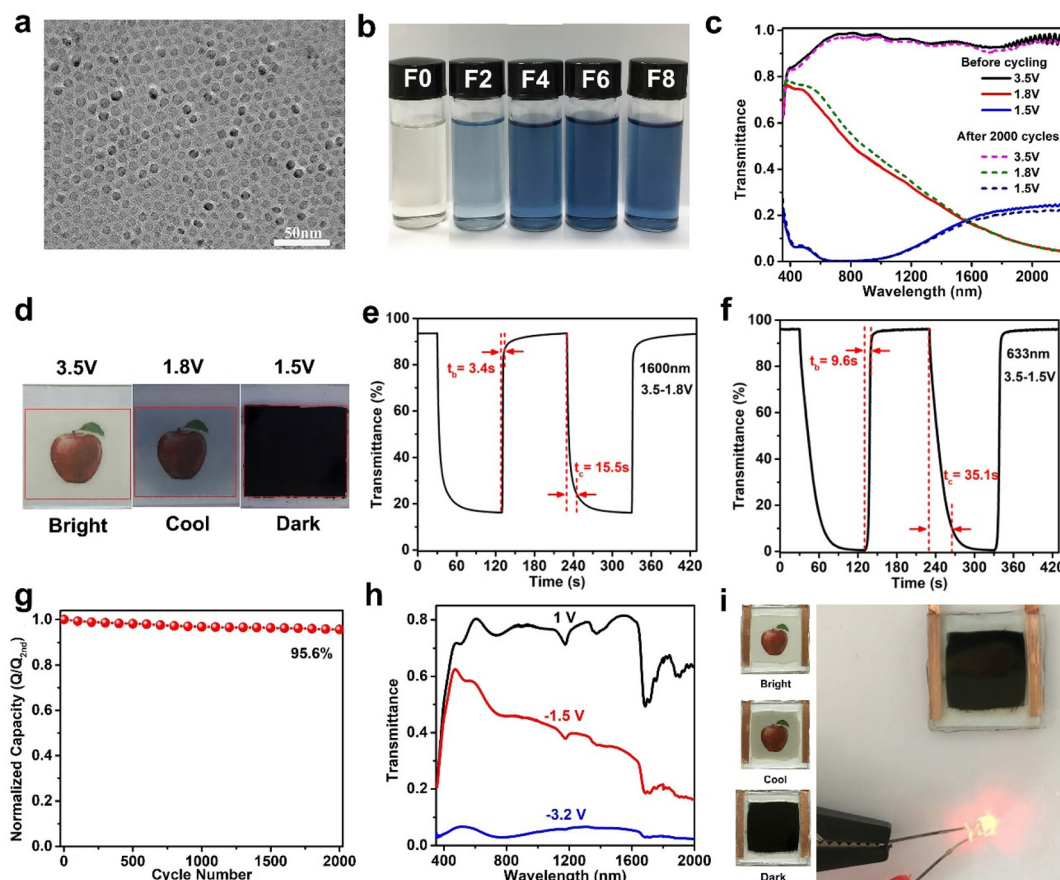


**Fig. 5** (a) TEM image and (b) digital photos of $TiO_{2-x}$ NCs. (c) Optical transmittance spectra, (d) digital photos, (e and f) switching speed, and (g) cycling stability of $TiO_{2-x}$ NC film. (h) Optical transmittance spectra and (i) digital photos of the dual-band EC device. Adapted with permission from ref. 64. Copyright 2020, Wiley-VCH.

absorbing the entire visible region (380–780 nm).[66] Recently, Cai *et al.* reported a porous self-supported NiO film prepared by a facile and low-cost electrostatic spray technology (Fig. 6a and b).[67] The fabricated NiO NCs films exhibited high transparency and black colors and realized a large optical modulation of 83.2% at 550 nm, high coloration efficiency (75.5 cm$^2$ C$^{-1}$), and superior energy storage capacity (Fig. 6c and d). This self-supported NiO film had also been further developed to fabricate transmissive-to-black device with TiO$_2$ nanoparticles film and 1 M KOH/PVA electrolyte (Fig. 6e). Originally, as the temperature increased, the device presented higher optical modulation and achieved 74% of optical modulation at 60 °C, indicating good thermal stability (Fig. 6f). Moreover, the

device possessed energy storage capacity and could light up LED easily (Fig. 6g and h).

**2.1.4. 0D niobium tungsten oxides.** Niobium tungsten oxides (Nb$_{18}$W$_{16}$O$_{93}$) have recently attracted increasing attention owing to their superstructures. Nb$_{18}$W$_{16}$O$_{93}$ is composed of corner- and edge-shared NbO$_6$ and WO$_6$ octahedra and partially filled with –W–O– chains, which forms a large number of tunnels and allows ions to pass through rapidly (Fig. 6i).[68] Therefore, Nb$_{18}$W$_{16}$O$_{93}$ shows a high ion diffusion coefficient and excellent stability. Recently, Cai *et al.* proposed a novel multistep strategy to enhance the electrochromic properties of EC devices by implementing the adsorption/desorption, insertion/extraction, and reversible electrodeposition of Zn$^{2+}$ on the
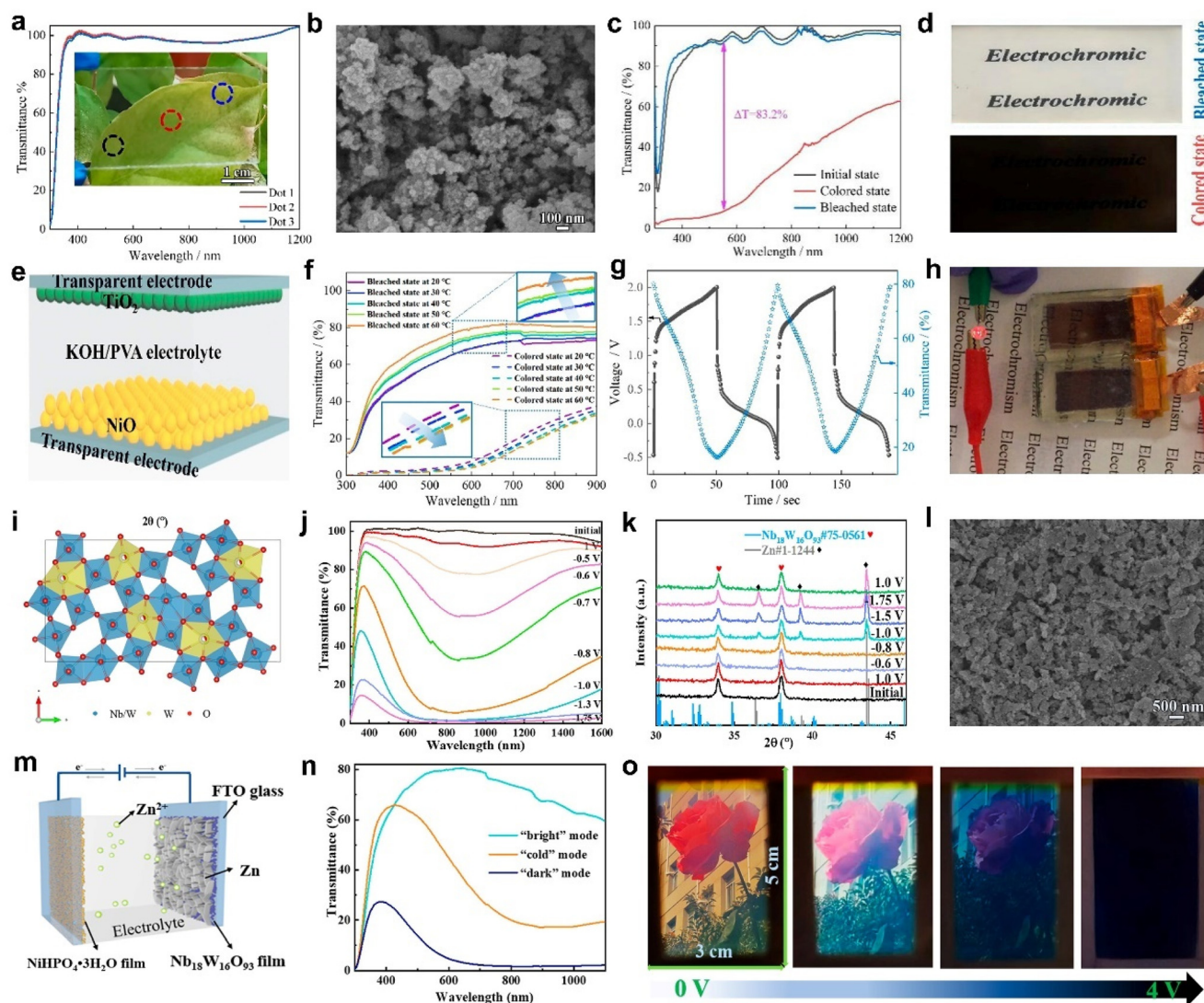


**Fig. 6** (a) The transmittance spectra of the NiO film at three different points. (b) SEM image of the as-prepared NiO powder. (c) The transmittance spectra and (d) digital photographs of the NiO film in the coloration and bleaching states. (e) Configuration structure, (f) transmittance spectra, (g) charge–discharge curve, and (h) powering an LED of the electrochromic energy storage device. (a–h) Adapted with permission from ref. 67. Copyright 2023, American Chemical Society. (i) Top view of the crystal structure model of Nb$_{18}$W$_{16}$O$_{93}$. (j) Transmittance spectra, (k) XRD patterns of Nb$_{18}$W$_{16}$O$_{93}$ films at different potentials. (l) SEM image of Nb$_{18}$W$_{16}$O$_{93}$ films after 3500 cycles. (m) Schematic illustration, (n) transmittance spectra, and (o) digital photos of the EC device based on Nb$_{18}$W$_{16}$O$_{93}$ films. (i–o) Adapted with permission from ref. 68. Copyright 2023, American Chemical Society.

$Nb_{18}W_{16}O_{93}$ electrochromic film.[69] $Nb_{18}W_{16}O_{93}$ NCs film (Fig. 6j) was prepared by spray coating, which demonstrated the wide-band optical modulation over the VIS-NIR range (87.0%, 96.2%, and 92.8% at 400, 633, and 1200 nm, respectively). As shown in Fig. 6k, when the voltage was applied to −1 V, the XRD peaks of the film began to show the characteristic peaks of Zn, indicating the nucleation and growth of the Zn layer on the $Nb_{18}W_{16}O_{93}$ film. The films with $Zn^{2+}$ deposition demonstrated higher coloration efficiency (72.4 and 103.7 $cm^2$ $C^{-1}$ at 633 and 1200 nm, respectively), compared to films without $Zn^{2+}$ deposition (45 and 60.8 $cm^2$ $C^{-1}$ at 633 and 1200 nm, respectively). After 3500 cycles, the structure of the film became loose and porous, which improved the ion transfer kinetics (Fig. 6l). Furthermore, a demonstrating device (Fig. 6m–o) was fabricated and exhibited independent control of the VIS and NIR transmittance and fast switching speed (12.9 s for coloring, 40.4 s for bleaching).

## 2.2. One-dimensional (1D) inorganic EC materials

One dimensional (1D) nanomaterials mainly refer to the nanowires, nanorods, nanofibers, and nanoribbons. Their diameter is controlled within 1 and 100 nm, while their length can be several micrometers, even up to hundreds of micrometers or a few millimeters. The large aspect ratio of 1D nanomaterials is beneficial for transporting ions and electrons rapidly, thus improving the EC properties. In addition, 1D nanomaterials are easy and suitable for fabricating high-quality thin films. Consequently, a variety of 1D inorganic materials have been developed and studied for EC applications. The recent progress of 1D inorganic EC materials is summarized in the following sections.

**2.2.1. 1D tungsten oxides.** 1D tungsten oxide ($WO_x$) is one of the most typical and promising candidate materials in current electrochromic devices because of their impeccable
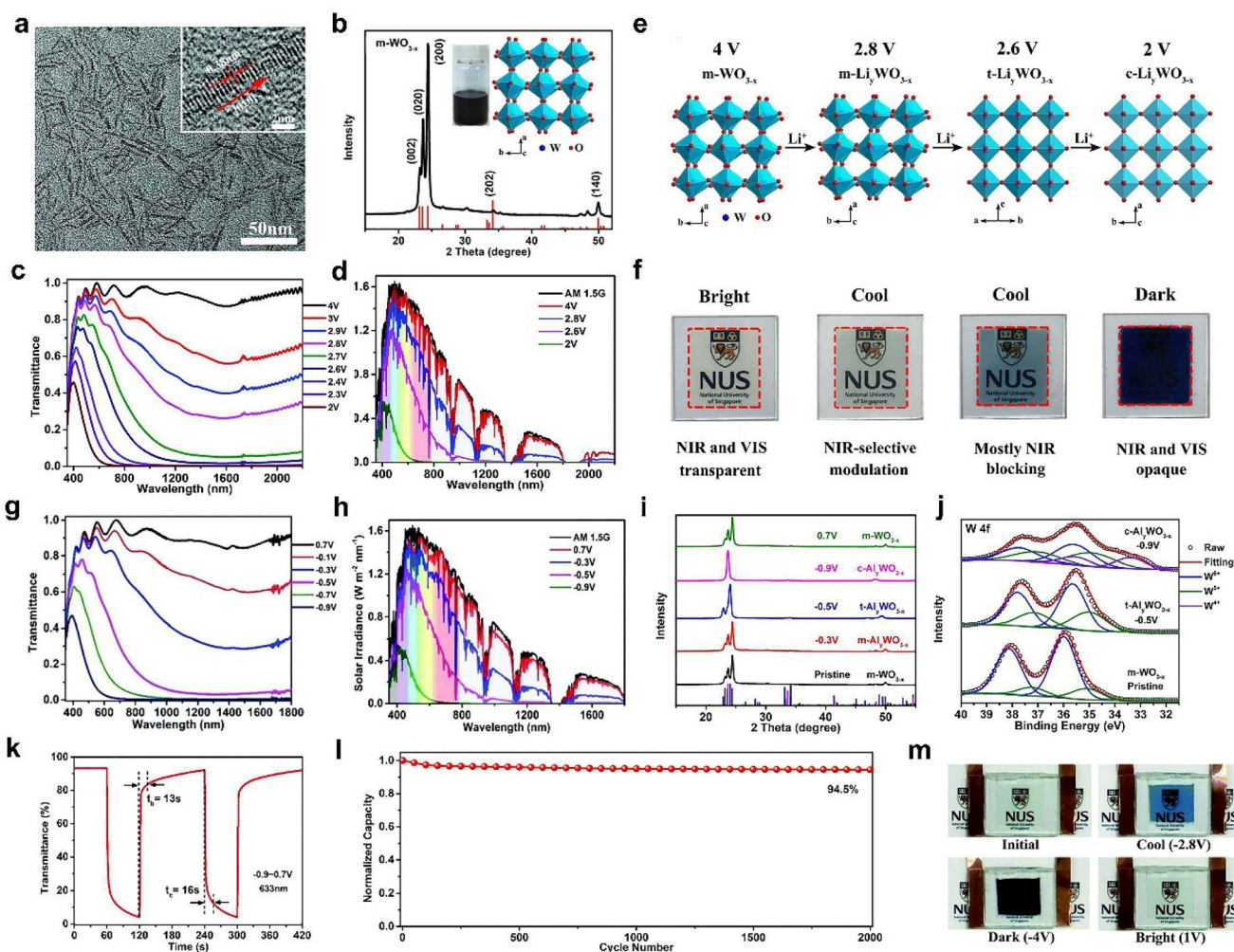


**Fig. 7** (a) TEM image, (b) XRD pattern of m-$WO_{3-x}$ NWs. (c) Optical transmittance spectra, (d) solar irradiance spectra of the m-$WO_{3-x}$ NW film. (e) Crystal structures and (f) corresponding photos of m-$WO_{3-x}$ NW films at 4 V, 2.8 V, 2.6 V., and 2 V (vs. $Li^+/Li$), respectively. (a–f) Adapted with permission from ref. 44. Copyright 2018, Royal Society of Chemistry. (g) Transmittance spectra, (h) solar irradiance spectra, (i) XRD patterns, (j) W 4f XPS spectra, (k) switching speed, (l) cycling stability of m-$WO_{3-x}$ NW films in $Al^{3+}$-based electrolyte. (m) Digital phots of the $Al^{3+}$-based device. (g–m) Adapted with permission from ref. 61. Copyright 2018, Royal Society of Chemistry.

performance in different fields. Recently, Zhang *et al.*[44] prepared a new monoclinic oxygen-deficient tungsten oxide nanowires (m-WO$_{3-x}$ NWs) by the colloidal method (Fig. 7a and b). Due to the abundant oxygen vacancies, the m-WO$_{3-x}$ NWs showed strong LSPR absorption in the entire NIR region, which is beneficial to the NIR-selective modulation. They not only demonstrated that dynamic and independent control of NIR and VIS light is possible with a single-component m-WO$_{3-x}$ NWs (Fig. 7c and d) without the need for compositing with other electrochromic materials but also presented a systematic investigation of the underlying dual-band electrochromic mechanism. A localized surface plasmon resonance and phase-transition assisted mechanism and bandgap transition electrochromism were individually responsible for the modulation of the NIR and VIS light transmittance (Fig. 7e and f). For further improving the switching speed and cycling stability, Zhang *et al.*[61] presented a dual-band electrochromic smart window design based on the intercalation/de-intercalation of Al$^{3+}$ cations to replace the common use of monovalent cations in electrochromic applications. The Al$^{3+}$ intercalation/de-intercalation-enabled electrochromic smart window delivered not only an efficient and independent control of NIR and VIS light transmittance but also an impressive electrochromic performance (Fig. 7g–l)—a high optical modulation of the full solar spectrum (93.2%, 91.7%, 88.5%, and 86.8% at 633, 800, 1200, and 1600 nm, respectively), high coloration efficien-
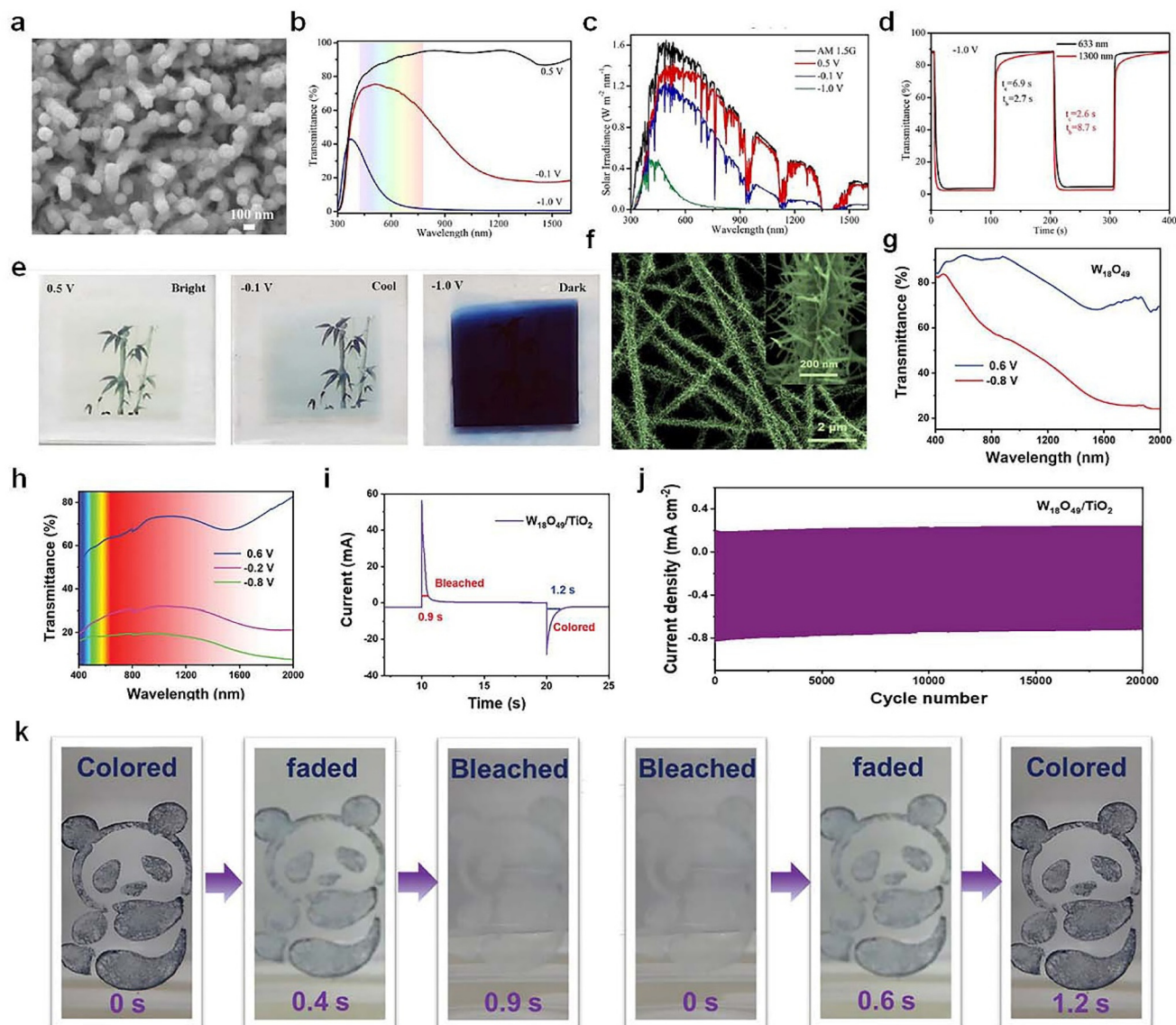


**Fig. 8** (a) SEM image, (b) optical transmittance spectra, (c) solar irradiance spectra, (d) switching speed, and (e) digital photos of the WO$_3$ NWs/NPs film. (a–e) Adapted with permission from ref. 70. Copyright 2023, American Chemical Society. (f) SEM image of the W$_{18}$O$_{49}$/TiO$_2$ heterostructures. Transmittance spectra of (g) W$_{18}$O$_{49}$ nanowires and (h) PNL-W$_{18}$O$_{49}$/TiO$_2$ heterostructures. (i) Switching speed, (j) cycling stability, and (k) optical images of W$_{18}$O$_{49}$/TiO$_2$ heterostructures. (f–k) Adapted with permission from ref. 71. Copyright 2022, Wiley-VCH.

cies, fast switching times (8/5 s and 16/13 s at 1200 and 633 nm, respectively, for coloration/bleaching), and high bistability and cyclability (5.5% capacity loss after 2000 cycles). The good electrochromic performance can be attributed to the effective diffusion of $Al^{3+}$ in the electrochromic material and a shallow intercalation/de-intercalation depth enabled by the ability of $Al^{3+}$ to support three-electron redox reactions. The performance of $Al^{3+}$ intercalation/de-intercalation-enabled dual-band electrochromism was also verified in laboratory prototype devices (Fig. 7m) to confirm its suitability for dual-band smart windows.

As shown in Fig. 8a–e, Cai et al.[70] recently prepared a type of porous $WO_3$ film with nanowires/nanoparticles core/shell architecture as a promising candidate for smart windows with a dual-band electrochromic feature. The results indicated that the dual-band electrochromic performance was credited to the progressive electrochemical reduction procedure, in which the capacitive charging process gave rise to NIR regulation and the following ion intercalation contributed to VIS light modulation. Inspired by pine needles, Zhang et al.[71] synthesized a unique pine-needle-like (PNL) $W_{18}O_{49}/TiO_2$ heterostructure (Fig. 8f), which was constructed with $W_{18}O_{49}$ nanowires (as branches) and $TiO_2$ nanofibers (as backbones). The PNL-$W_{18}O_{49}/TiO_2$ heterostructures exhibited superior dual-

band EC performance in both VIS and NIR bands (Fig. 8h–k), which can block up to 81.4% of the VIS light at 633 nm and they also showed extremely short bleaching/coloring time (0.9/1.2 s) and excellent stability (85% of capacity retention after 20 000 cycles).

Zn is abundant, safe, easily processed in aqueous electrolytes and provides two electrons during redox reactions, which is conductive for triggering electrochromism via $Zn^{2+}$ intercalation. Li et al.[72] recently reported a Zn-based electrochromic battery utilizing the Ti-substituted tungsten molybdenum oxide (MTWO, Fig. 9a) nanowires. Ti-doping clearly enhanced the intercalation of $Zn^{2+}$, yielding improved capacity and electrochromic performance (Fig. 9c–d). The Zn-based electrochromic batteries (Fig. 9e and f) exhibited an areal capacity of 260 mA h m$^{-2}$ and high optical contrast (76%). Gao et al.[73] reported an electro-chromic-chemical device (MED) in large area made of $W_{17}O_{47}$ nanowires, where $Zn^{2+}$ ion intercalation took place in the oxygen-vacancy monoclinic $WO_3$ with WO polyhedral. The large-area MEDs assembled with $W_{17}O_{47}/NaWO_3$ NW electrodes (Fig. 9g) exhibited excellent energy-saving and energy-storage properties. The $W_{17}O_{47}/NaWO_3$ electrode materials exhibited excellent high optical modulation and fast switching speed (Fig. 9h and i). Furthermore, a large area Zn-based MED assembled with the $W_{17}O_{47}/NaWO_3$ NW
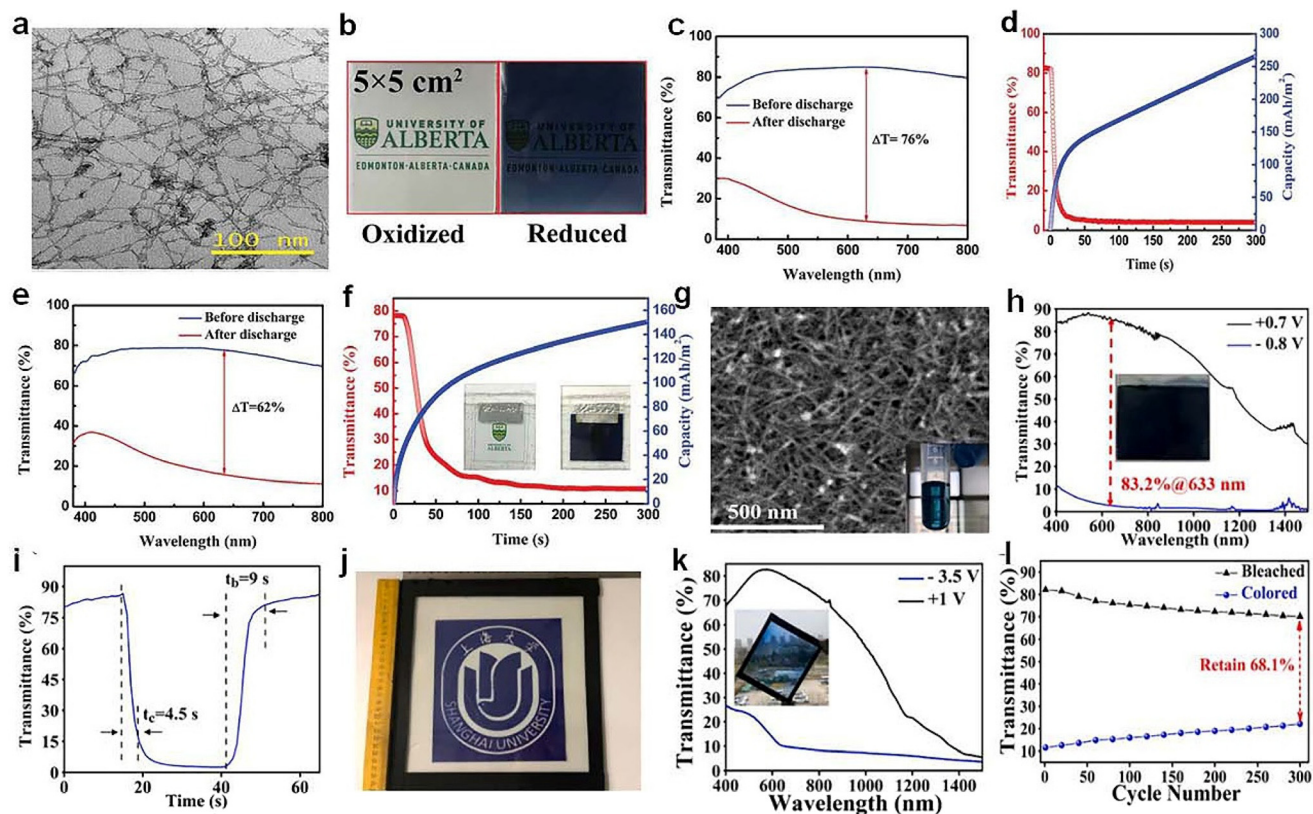


Fig. 9 (a) TEM image of the MTWO. (b) Photographs, (c) transmittance spectra, and (d) self-coloring (discharge) process of a MTWO cathode. (e) Transmittance spectra, (f) self-coloring process of the Zn-based EC device. (a–f) Adapted with permission from ref. 72. Copyright 2019, Wiley-VCH. (g) SEM image, (h) transmittance spectra, (i) switching speed of $W_{17}O_{47}/NaWO_3$ NW electrode. (j) Photograph, (k) transmittance spectra, and (l) cycling stability of the prototype MED. (g–l) Adapted with permission from ref. 73. Copyright 2021, Elsevier.

electrode (30.5 cm × 26 cm, Fig. 9j) was demonstrated in a model window, which also showed high electrochromic performance and good stability, suggesting the great potential of Zn-based MED based on $W_{17}O_{47}/NaWO_3$ NWs.

Co-assembly of various nanowires represents a promising technology for fabricating next-generation multifunctional electronics. For example, Yu et al.[74] demonstrated a novel mul-

ticolor electrochromic device by co-assembling $W_{18}O_{49}$ and $V_2O_5$ NWs using solution-based Langmuir–Blodgett (LB) technique (Fig. 10a and b). The transparent $W_{18}O_{49}/V_2O_5$ NW film showed a dynamic color change (orange, green, and gray) by controlling the applied voltages (Fig. 10c and d). Both the transmittance and color of the device can be easily controlled by manipulating the layers of co-assembled NWs and the
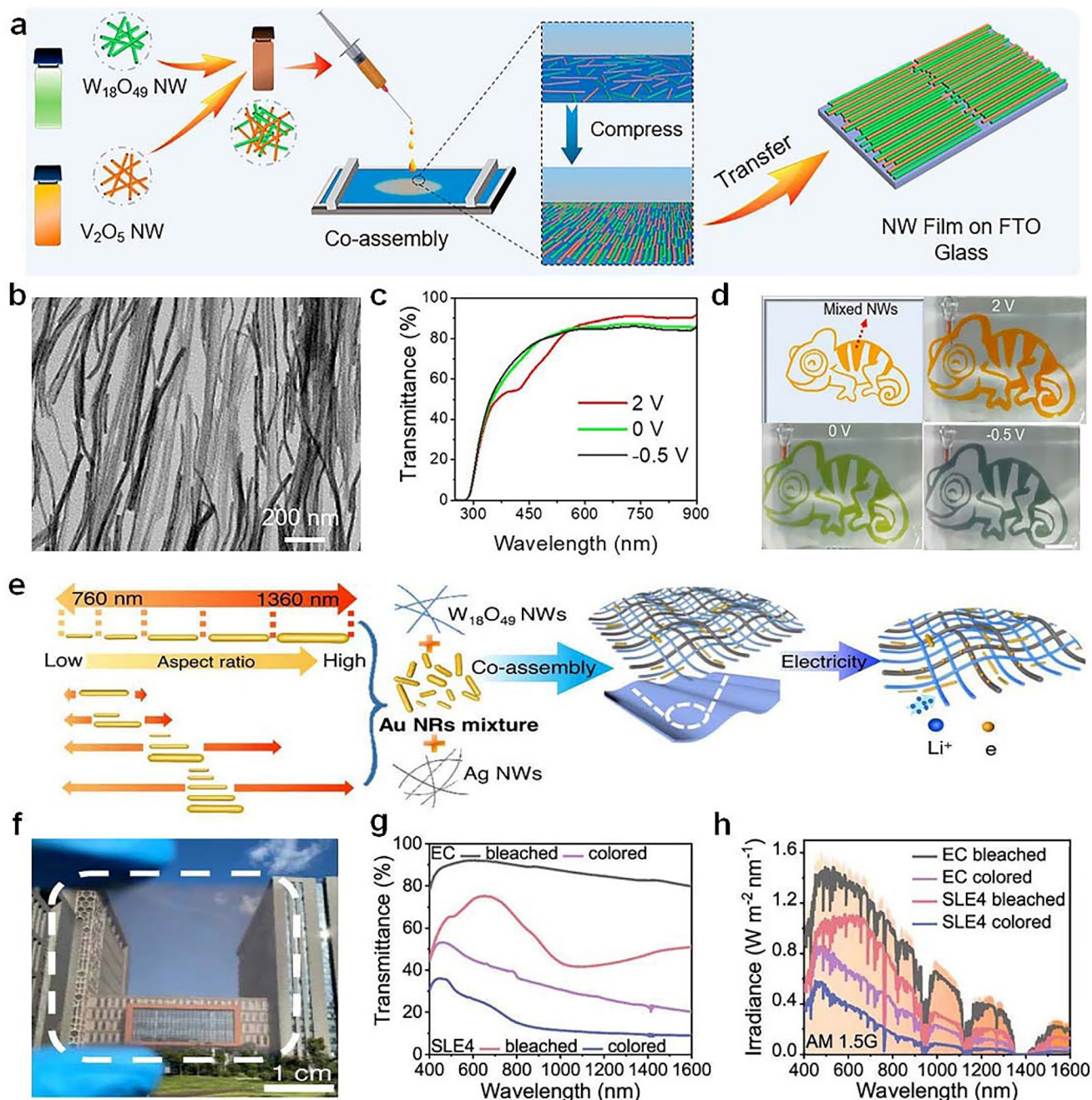


Fig. 10   (a) Schematic illustration for co-assembling $W_{18}O_{49}$ and $V_2O_5$ NWs based on LB technique. (b) TEM image, (c) optical transmittance spectra, and (d) digital photos of the as-prepared $W_{18}O_{49}/V_2O_5$ NW film. (a–d) Adapted with permission from ref. 74. Copyright 2021, American Chemical Society. (e) Schematic illustration on the co-assembly of $W_{18}O_{49}$ nanowires and Au nanorods. (f) Digital photo, (g) optical transmittance spectra, and (h) solar spectral irradiance of the prepared $W_{18}O_{49}/Au$ films. (e–h) Adapted with permission from ref. 75. Copyright 2023, Springer Nature.

ratios between the two NWs. Recently, Yu et al.[75] used the co-assembly strategy to fabricated the selective light absorption electrochromic (SLE) smart window by integrating $W_{18}O_{49}$ NWs and Au nanorods (Fig. 10e). The prepared $W_{18}O_{49}$/Au films exhibited enhanced EC performance (Fig. 10f–h), especially for NIR-selective modulation due to the strong LSPR of Au, which significantly improved the cooling efficiency of EC windows.

**2.2.2. 1D vanadium oxides.** Vanadium oxides ($V_2O_5$), a classic inorganic electrochromic material, has recently intrigued significant attention due to its multicolor and bipolar properties, showing application potential in new energy-saving displays. Recently, Li et al.[76] demonstrated a transparent inorganic multicolor display platform by sandwiching the Zn anode between two sodium vanadium oxide (SVO) nanorod cathode (Fig. 11a–d). This display could be reversibly switched between multiple colours (orange, amber, yellow, brown, char-

treuse, and green) while preserving a high optical transparency, as shown in Fig. 11e–g. In addition, they[77] recently prepared potassium vanadate nanorods ($K_2V_6O_{16}\cdot1.5H_2O$, KVO, Fig. 11h and j) and reported a zinc-anode-based multicolor transparent electrochromic display with high stability (Fig. 11j–n) utilizing a hybrid electrolyte consisting of tetraethylene glycol dimethyl ether (TEGDME) and water. Furthermore, the KVO showed superior electrochromic performance compared to SVO due to the wide KVO interlayer spacing.

### 2.3. Two-dimensional (2D) inorganic EC materials

Two-dimensional (2D) materials are sheet-like nanomaterials composed of single or multiple layers of atoms or molecules. Its transverse size can reach tens of microns or even larger. 2D materials exhibit unusual physicochemical properties due to their unique internal structure.[78] The surface atoms of 2D
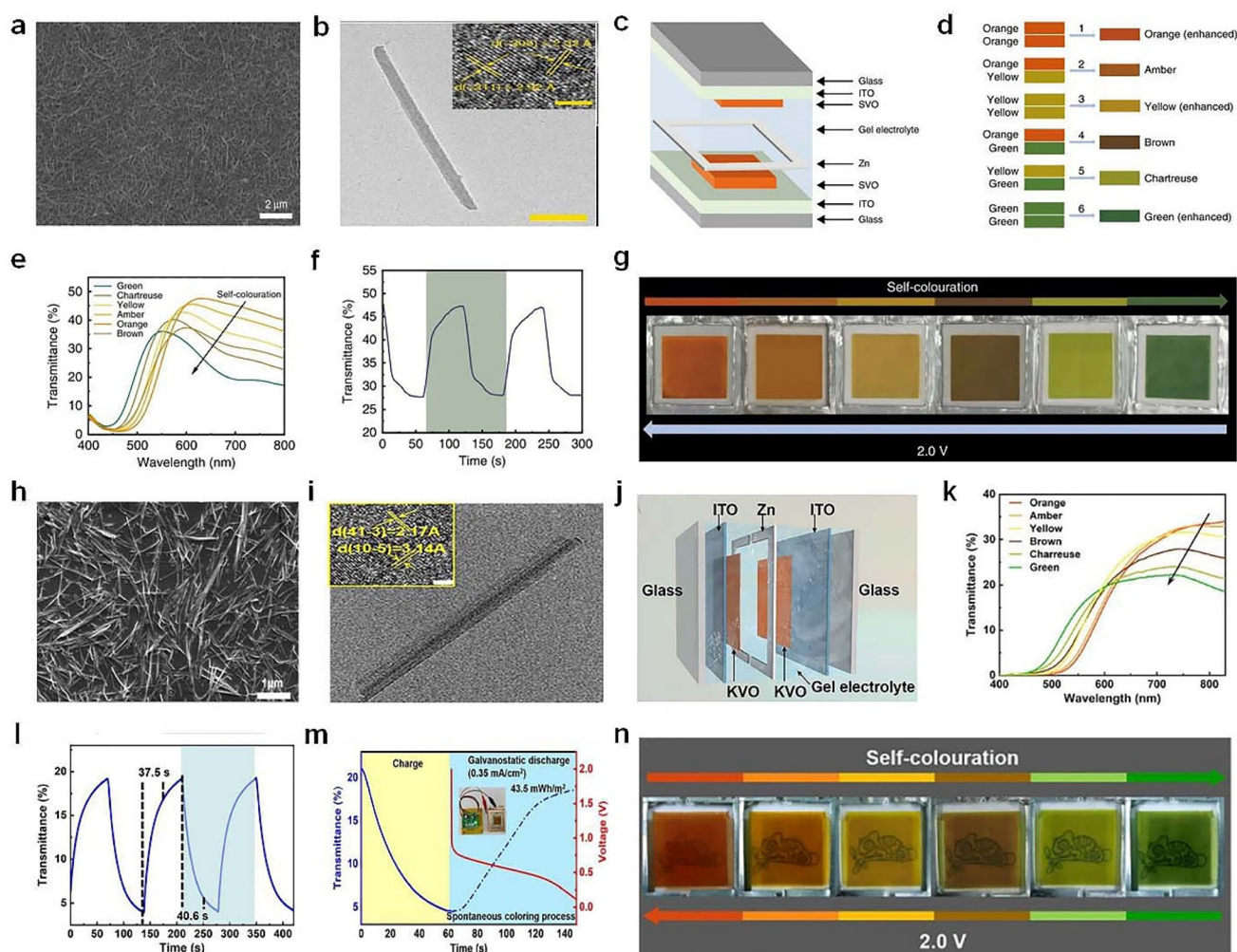


**Fig. 11** (a) SEM and (b) TEM images of the SVO nanorods. (c) Schematic illustration of Zn–SVO EC display and (d) the color overlap effect. (e) Transmittance spectra, (f) switching time, (g) digital photos of the Zn–SVO device under different voltages. (a–g) Adapted with permission from ref. 76. Copyright 2020, Springer Nature. (h) SEM and (i) TEM images of the KVO nanorods. (j) Schematic diagram, (k) optical transmittance spectra, (l) switching speed, (m) energy-recycling performance, and (n) digital photos of the Zn–KVO EC display. (h–n) Adapted with permission from ref. 77. Copyright 2023, Wiley-VCH.

materials are almost completely exposed and the utilization rate of the atoms is greatly improved. By stacking layers and mixing elements, it is easier to adjust the band structure and performance. Atomic thickness brings excellent flatness and structural stability, and ultrathin thickness gives excellent bending properties to 2D materials, making them the first choice for flexible EC devices.

**2.3.1. 2D tungsten oxides.** 2D nanosheets have been found to significantly increase the surface area and ionic diffusivity of the EC materials, resulting in the faster switching speeds. For example, Ashraful Azam et al.[79] successfully prepared 2D $WO_3$ nanosheets (Fig. 12a and b) by peeling and oxidizing the layered $WS_2$ powder. These nanosheets were then dispersed in a solution and used to form uniform films through simple casting. The resulting electrochromic devices (Fig. 12c and d) showed an optical modulation of 62.57%, which was 3.43 times higher than devices using bulk $WO_3$ powder. Additionally, the switching response time was improved by approximately 46.62% for coloration and 62.71% for bleaching, which can be attributed to the high surface area and fast ion diffusion coefficient of 2D $WO_3$ nanosheets.

**2.3.2. 2D titanium dioxides.** Among many transition metal oxides, $TiO_2$ nanosheets have great potential in the field of EC due to their low cost, stable properties, and other advantages. Recently, Wang et al.[80] reported a 2D $TiO_2$ nanosheets

(Fig. 12e and f) by annealing 2D $Ti_3C_2T_x$ aerogel in air and also demonstrated flexible, fast, and high-coloration-efficiency EC devices based on self-assembled 2D $TiO_2$ (Fig. 12g). Benefiting from the well-balanced porosity and connectivity of these assembled nanometer-thick heterostructures, they presented fast and efficient ion and electron transport, as well as superior mechanical and electrochemical stability. In addition, they further demonstrated large-area flexible devices (Fig. 12h and i), which could potentially be integrated onto curved and flexible surfaces for future ubiquitous electronics.[80]

**2.3.3. 2D Graphene.** Graphene, as the first 2D material discovered, has been widely studied and applied in the field of energy storage, catalysis, optoelectronics, etc., due to its excellent physical, electrical, optical, and mechanical properties. Kocabas et al.[18] used multilayer graphene as the EC layer and fabricated a novel IR EC device, which could dynamically modulate the IR emissivity by varying the applied voltages (Fig. 13a–c). When applying a voltage bias, the ionic liquid intercalated into the graphene layers as a result of doping, the charge density on graphene increased and the Fermi-level shifted to higher energies, which suppressed the IR absorption and thus the emissivity of the graphene electrode. Based on the intercalation/de-intercalation of ionic liquid, the IR emissivity of multilayer graphene electrodes can be tuned between 0.8 and 0.3 (Fig. 13d–f), showing potentials in adaptive
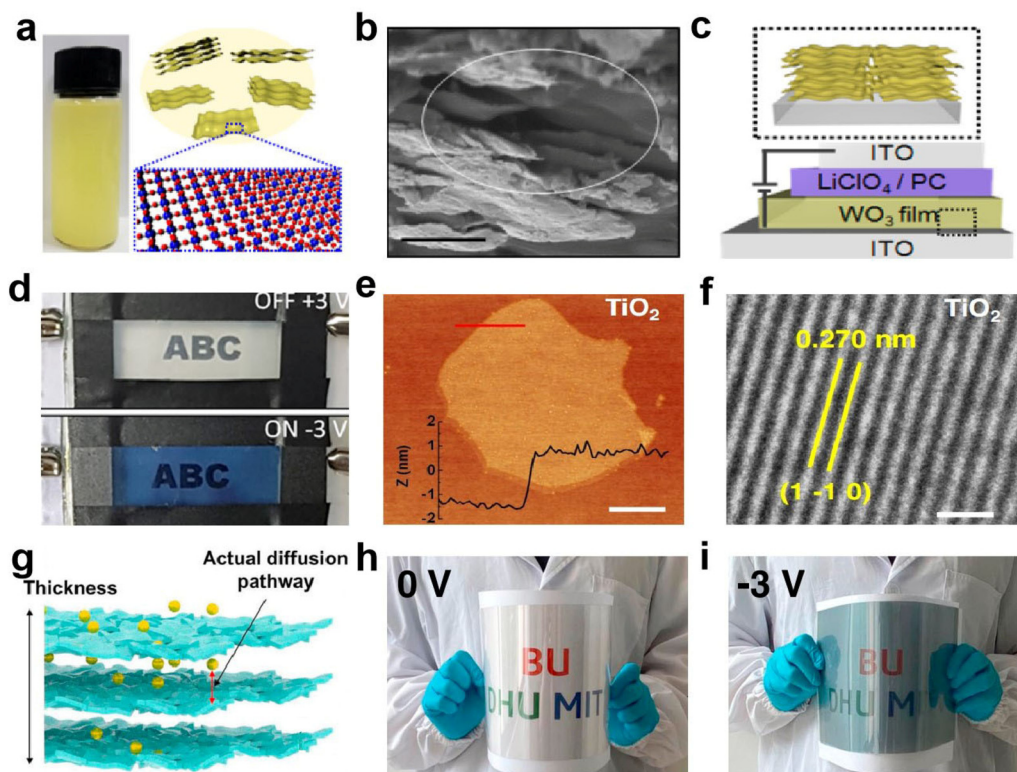


**Fig. 12** (a) Schematic diagram and (b) SEM image of 2D $WO_3$ nanosheets. (c) Schematic diagram and (d) digital photos of the EC device based on $WO_3$ nanosheets. (a–d) Adapted with permission from ref. 79. Copyright 2018, American Chemical Society. (e) AFM and (f) HRTEM images of $TiO_2$ sheet. (g) Schematic diagram of self-assembled 2D $TiO_2$ films. (h and i) The digital photos of the large-area device in the bent state. (e–i) Adapted with permission from ref. 80. Copyright 2021, Springer Nature.
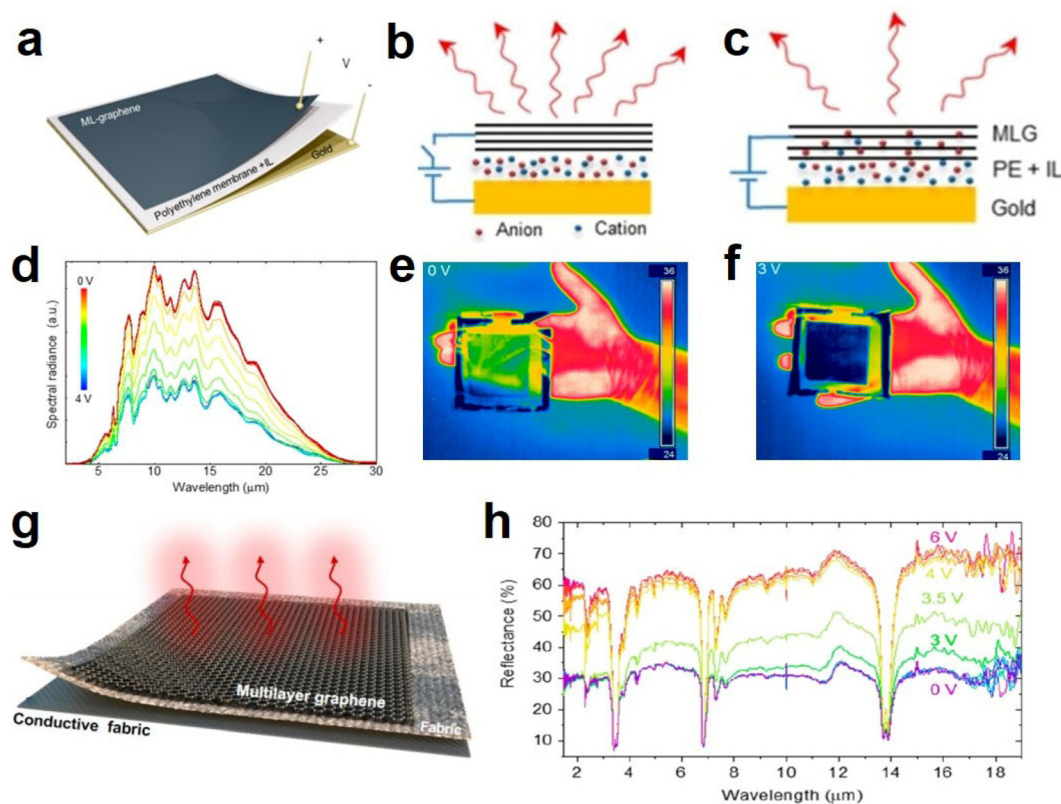
**Fig. 13** (a) Structure diagram, (b and c) principal diagram of graphene-based device. (d) Spectra of the thermal radiation from the graphene-based device at voltages. (e and f) Thermal camera images of device at 0 V and 3 V. (a–f) Adapted with permission from ref. 18. Copyright 2018, American Chemical Society. (g) Schematic diagram of the textile device with various laminated layers. (h) Infrared reflectance spectra of the textile at different voltages. (g and h) Adapted with permission from ref. 19. Copyright 2020, American Chemical Society.

thermal camouflage. Subsequently, Kocabas *et al.*[19] fabricated adaptive IR textiles by incorporating graphene into clothing fabrics. The device consisted of an IR transparent polymer layer, a CVD-grown multilayer graphene (MLG) layer, a fabric separation layer, and a conductive fabric layer (Fig. 13g). The demonstrated IR textile device showed a variable IR emissivity performance (Fig. 13h), which exhibited promising application in wearable and adaptive suits. The properties and functions of graphene are irreplaceable in some areas and even regarded as the future direction, but the expensive synthesis price and difficult transfer methods also limit its development. In the future, the industrialization and commercialization of graphene will be a long process.[81]

**2.3.4. 2D MXene.** MXenes are a large family of 2D metal carbides and nitrides and have been widely studied due to excellent electronic, optical, mechanical, and electrochemical properies.[82] As a novel 2D material, MXene has recently been studied for EC applications. Han *et al.*[83] reported an IR EC device based on MXene nanosheets for dynamic thermal radiation regulation, demonstrating the capability of dynamic IR emissivity modulation of MXene (Fig. 14a–c). They also revealed that the reason for MXene emissivity variation was related to the changes in the free O-terminal groups caused by Li+ intercalation/de-intercalation. With excellent electronic/ion

conductivity and high mechanical strength, MXene can be used as flexible electrode materials for electrochemical actuators. Recently, Gogotsi *et al.*[84] reported an EC actuator using MXene (Fig. 14d and e), which exhibited a high curvature (0.083 mm$^{-1}$) and strain (0.29%). In addition, the MXene-based EC actuator with a symmetric configuration also had curvature and strain variations of up to 0.038 mm$^{-1}$ and 0.26% with excellent retention after 10 000 cycles (Fig. 14f–h). They also revealed the actuation mechanism, which can be attributed to the expansion and contraction of the MXene layer spacing.

## 3. Summary and prospects

With the rapid development of EC and nanoscience fields, significant progress has been made on advanced inorganic EC nanomaterials and devices for light and thermal management in the past few years. In this review, we systematically summarize and discuss the recent advances in advanced inorganic EC nanomaterials, mainly focusing on low dimensional transition metal oxides (*e.g.*, $WO_3$, $TiO_2$, $NiO$, $Nb_{18}W_{16}O_{93}$, and $V_2O_5$), graphene, and MXenes (Table 1). Taking advantages of the short ion diffusion distance, fast ion diffusion speed, and high
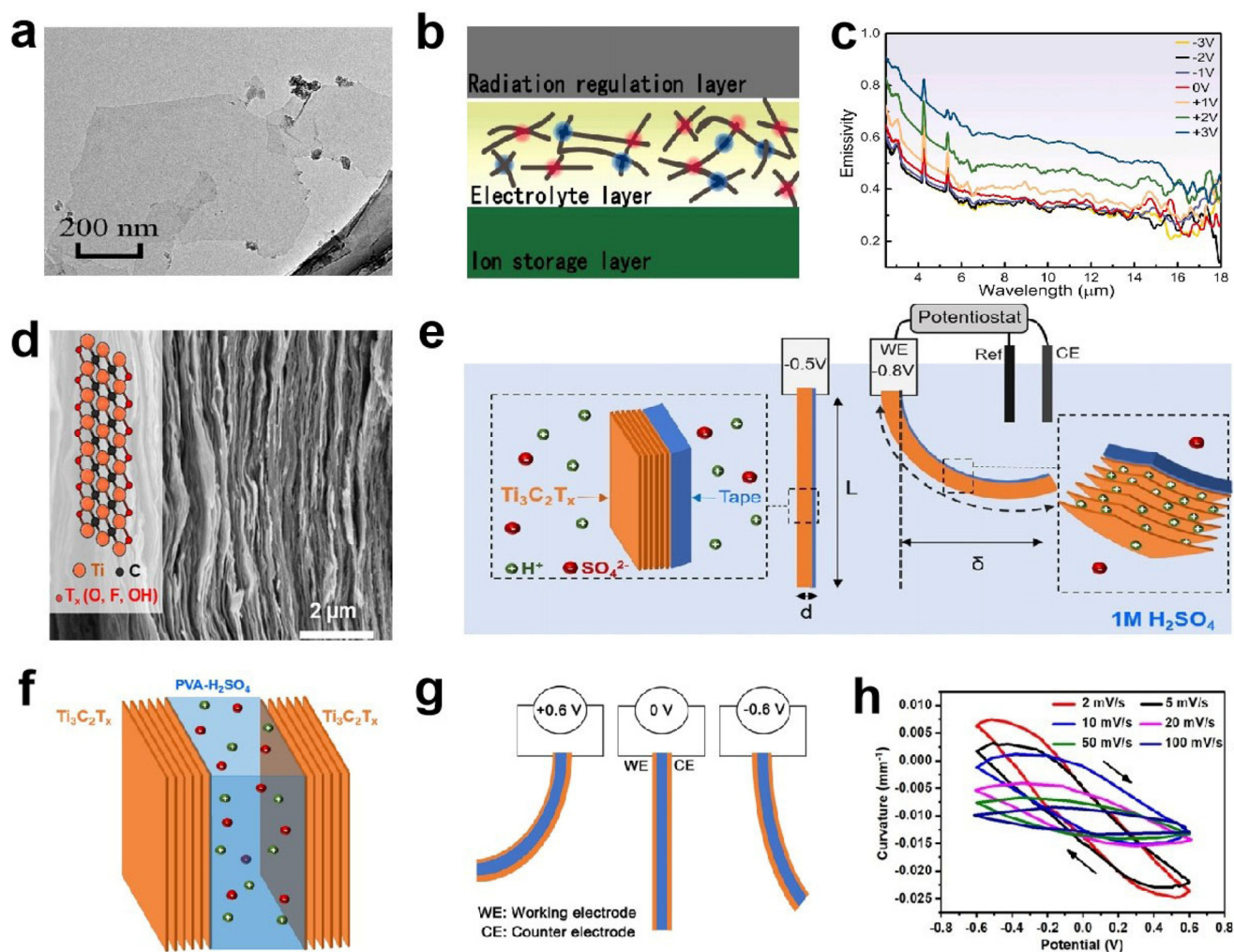
**Fig. 14** (a) HRTEM image of MXene nanosheets. (b) Structure and (c) emissivity of the MXene-based EC device. (a–c) Adapted with permission from ref. 83. Copyright 2022, Elsevier. (d) Cross-sectional SEM image of a $Ti_3C_2T_x$ electrode. (e) Schematic representation of the EC film. (f and g) The configuration and (h) curvature of the EC actuator. (d–h) Adapted with permission from ref. 84. Copyright 2019, American Chemical Society.

**Table 1** Comparison of the EC performance of recent advanced inorganic EC nanomaterials ($\Delta T_{633nm}$ is the optical modulation at 633 nm; $t_c/t_b$ is the coloration/bleaching time; CE is coloration efficiency; N/A indicates not available)

| Material | $\Delta T_{633nm}$ | $t_c/t_b$ (s) | CE (cm$^2$ C$^{-1}$) | Cycle stability | Ref. |
|---|---|---|---|---|---|
| NbO$_x$-WO$_{3-x}$ NC film | ~80% | 600/100 | N/A | 2000 cycles (5.7% capacity loss) | 36 |
| Ti-WO$_3$ NC film | 84.9% | 3.3/25 | 114.9 | 1000 cycles (11% optical loss) | 48 |
| WO$_3$ QD film | Li$^+$: 97.8% | Li$^+$: 4.5/4 | Li$^+$: 76.8 | Li$^+$: 10 000 cycles (10% optical loss) | 50 |
| | Al$^{3+}$: 94.1% | Al$^{3+}$: 13.5/10 | Al$^{3+}$: 82.9 | Al$^{3+}$: 20 000 cycles | |
| WO$_{3-x}$ NC device | 76% | 4.5/3.7 | 97.7 | 1000 cycles (30% capacity loss) | 55 |
| Ta-TiO$_2$ NC film | ~90% | 66.8/6.9 (550 nm) | 33.2 (550 nm) | 2000 cycles (14.8% capacity loss) | 57 |
| W-TiO$_2$ NC device | 77% | 7.9/5.8 | 37.3 (550 nm) | 1000 cycles (8.9% capacity loss) | 42 |
| TiO$_{2-x}$ NC film | 95.5% | 15.5/3.4 | 38.2 | 2000 cycles (4.4% capacity loss) | 64 |
| NiO NC film | ~75% | N/A | 75.5 (550 nm) | N/A | 67 |
| Nb$_{18}$W$_{16}$O$_{93}$ NC film | 96.2% | 7/29 | 72.4 | 3500 cycles (28% optical loss) | 68 |
| m-WO$_{3-x}$ NW film | Li$^+$: 91.7% | Li$^+$: 21/85 | Li$^+$: 101.7 | Li$^+$: 1000 cycles (20% capacity loss) | 44 |
| | Al$^{3+}$: 93.2% | Al$^{3+}$: 16/13 | Al$^{3+}$: 121 | Al$^{3+}$: 2000 cycles (5.5% capacity loss) | 61 |
| WO$_3$ NWs/NPs film | 87.1% | 6.9/2.7 | 79.2 | 1000 cycles (32.3% optical loss) | 70 |
| MTWO NW film | 76% | Self-coloration time: 14 | N/A | N/A | 72 |
| W$_{17}$O$_{49}$ NW film | 83.2% | 4.5/9 | N/A | 4000 cycles (25.7% optical loss) | 73 |
| W$_{18}$O$_{49}$ NW/Au film | ~50% | 4.5/4.0 | 48.46 | N/A | 75 |
| WO$_3$ Nanosheets device | ~51% | 10.74/6.97 (700 nm) | N/A | 1000 cycles (6% capacity loss) | 79 |
| TiO$_2$/Ti$_3$C$_2$T$_x$ Nanosheets film | ~48% | 1.71/0.3 (550 nm) | 243 | 1000 cycles (8% optical loss) | 80 |
| Graphene device | 43% (10 μm) | <1/<1 | N/A | 500 cycles | 18 |

surface area, nanomaterials not only notably improve the switching speed of EC process but also enhance the optical modulation and cycle stability of EC devices. Consequently, advanced inorganic EC materials have shown great potential applications in energy-saving smart windows, biostable displays, and adaptive thermal management.

Although significant achievements have been made, there are still some challenges in inorganic EC nanomaterials for practical applications.

(1) Mass preparation of inorganic EC nanomaterials: whether the inorganic EC nanomaterials with high quality and uniformity can be prepared in large quantities is a crucial factor for the future practical applications. Currently, a lot of synthetic methods such as solvothermal, sol–gel, colloidal, electrodeposition, and electrospinning have been developed for preparing high-quality nanomaterials. However, the mass of prepared nanomaterials is usually at the gram level, which is definitely not beneficial to practical application. For large-scale commercialization, mass preparation (at the kilogram level) of high-quality inorganic EC nanomaterials with a low-cost and facile process is essential.

(2) Low-cost and large-area film-forming technology: the high-quality film-forming technology with low-cost and large-area is another issue in the development of nanomaterial-based EC devices. The traditional EC film-forming technologies such as magnetron sputtering, vacuum evaporation, and spin-coating, which is either high-cost or small-area, are not suitable for next-generation EC devices with large-area and low-cost. Actually, a few other film-forming technologies such as automatic blade coating and roll-to-roll coating have been widely used in some other research fields (*e.g.*, batteries). These technologies might be able to address the current issue of electrochromic film preparation. However, the thickness of electrochromic film is only a few hundreds of nanometers, having a large difference with the thickness of battery electrodes (> dozens of micrometers). Consequently, how to acquire a high-uniform and high-quality electrochromic film using automatic blade coating or roll-to-roll coating is still a challenge, needing a long way to go for optimization and commercial production.

(3) Side reactions resulted from nanomaterials: although the high surface area of nanomaterials can increase the ion storage sites and contact area between the electrode and electrolyte, it can also cause some undesired side reactions such as catalyzing the decomposition of electrolyte due to the high reactivity. The decomposition of electrolyte will produce some gases such as carbon dioxide, causing the bubble issue of EC devices. Therefore, how to inhibit the side reactions is essential for the nanomaterial-based EC device. Besides the nanomaterials, the occurrence of side reactions is also related to the solid–liquid interface, electrolyte composition, electrode potential, and device structure. Consequently, interface designing, electrolyte optimization, reducing operating voltage, device structure design, and optimization are possible approaches to address the issue of side reaction.

Fortunately, more and more scientific and industrial researchers have started to conduct research works on electrochromism and try their best to address the problems of EC materials and devices. We suppose that significant breakthroughs will be achieved on nanomaterial-based EC devices in the near future. We also believe that the electrochromism technology will be widely used in our life and significantly improve the quality of our life in the future.

## Conflicts of interest

The authors declare no conflict of interest.

## Acknowledgements

## References

1 C. Gu, A. B. Jia, Y. M. Zhang and S. X. Zhang, *Chem. Rev.*, 2022, **122**, 14679–14721.

2 F. Zhao, B. Wang, W. Zhang, S. Cao, L. Liu, A. Y. Elezzabi, H. Li and W. W. Yu, *Mater. Today*, 2023, **66**, 431–447.

3 Z. Shao, A. Huang, C. Ming, J. Bell, P. Yu, Y.-Y. Sun, L. Jin, L. Ma, H. Luo, P. Jin and X. Cao, *Nat. Electron.*, 2022, **5**, 45–52.

4 Y. Ding, M. Wang, Z. Mei and X. Diao, *ACS Appl. Mater. Interfaces*, 2022, **14**, 48833–48843.

5 Y. Su, Y. Wang, Z. Lu, M. Tian, F. Wang, M. Wang, X. Diao and X. Zhong, *Chem. Eng. J.*, 2023, **456**, 141075.

6 Z. Zhou, Z. Chen, D. Ma and J. Wang, *Sol. Energy Mater. Sol. Cells*, 2023, **253**, 112226.

7 W. Zhao, J. Wang, B. Tam, H. Zhang, F. Li, A. Du and W. Cheng, *Adv. Opt. Mater.*, 2023, **11**, 2202774.

8 S. Zhang, Y. Peng, J. Zhao, Z. Fan, B. Ding, J. Y. Lee, X. Zhang and Y. Xuan, *Adv. Opt. Mater.*, 2022, **11**, 2202115.

9 S. Zhang, S. Cao, T. Zhang, Q. Yao, H. Lin, A. Fisher and J. Y. Lee, *Small Methods*, 2019, **4**, 1900545.

10 J. Chen, A. W. M. Tan, A. L.-S. Eh and P. S. Lee, *Adv. Energy Sustainability Res.*, 2021, **3**, 2100172.

11 Y. Wang, S. Wang, X. Wang, W. Zhang, W. Zheng, Y.-M. Zhang and S. X.-A. Zhang, *Nat. Mater.*, 2019, **18**, 1335–1342.

12 J. Chen, Y. Li, T. Zhang, X. Zha, X. Tang, X. Mu, P. Sun, G. Song, S. Cong, Q. Chen and Z. Zhao, *Laser Photonics Rev.*, 2022, **16**, 2200303.

13 Y. Li, P. Sun, J. Chen, X. Zha, X. Tang, Z. Chen, Y. Zhang, S. Cong, F. Geng and Z. Zhao, *Adv. Mater.*, 2023, **35**, 2300116.

14 H. Wei, J. Gu, F. Ren, L. Zhang, G. Xu, B. Wang, S. Song, J. Zhao, S. Dou and Y. Li, *Small*, 2021, **17**, e2100446.

15 W. Sun, X. Zhang, H. Zhang, Z. Ren, M. Chen, Y. Xiao, Z. Li, J. Deng, D. Yan, L. Zhang and Y. Li, *Laser Photonics Rev.*, 2023, **17**, 2300476.

16 H. Gong, W. Li, G. Fu, Q. Zhang, J. Liu, Y. Jin and H. Wang, *J. Mater. Chem. A*, 2022, **10**, 6269–6290.

17 L. Zhang, T. Hao, S. Song, B. Wang, D. Liu, Z. Ren, W. Liu, Y. Zhang, G. Xu, X. Yan, Y. Lu and Y. Li, *Chem. Eng. J.*, 2023, **475**, 145927.

18 O. Salihoglu, H. B. Uzlu, O. Yakar, S. Aas, O. Balci, N. Kakenov, S. Balci, S. Olcum, S. Suzer and C. Kocabas, *Nano Lett.*, 2018, **18**, 4541–4548.

19 M. S. Ergoktas, G. Bakan, P. Steiner, C. Bartlam, Y. Malevich, E. Ozden-Yenigun, G. He, N. Karim, P. Cataldi, M. A. Bissett, I. A. Kinloch, K. S. Novoselov and C. Kocabas, *Nano Lett.*, 2020, **20**, 5346–5352.

20 J. Guo, H. Jia, Z. Shao, P. Jin and X. Cao, *Acc. Mater. Res.*, 2023, **4**, 438–447.

21 J. Li, Y. Zhuang, J. Chen, B. Li, L. Wang, S. Liu and Q. Zhao, *Energy Chem.*, 2021, **3**, 100060.

22 Y. Huang, B. Wang, F. Chen, Y. Han, W. Zhang, X. Wu, R. Li, Q. Jiang, X. Jia and R. Zhang, *Adv. Opt. Mater.*, 2021, 2101783.

23 S. Kandpal, T. Ghosh, C. Rani, A. Chaudhary, J. Park, P. S. Lee and R. Kumar, *ACS Energy Lett.*, 2023, **8**, 1870–1886.

24 Q. Zhao, Z. Pan, B. Liu, C. Bao, X. Liu, J. Sun, S. Xie, Q. Wang, J. Wang and Y. Gao, *Nano-Micro Lett.*, 2023, **15**, 87.

25 X. Wu, Q. Fan, Z. Bai, Q. Zhang, W. Jiang, Y. Li, C. Hou, K. Li and H. Wang, *Small*, 2023, **19**, 2301742.

26 D. Zhang, J. Wang, Z. Tong, H. Ji and H. Y. Qu, *Adv. Funct. Mater.*, 2021, **31**, 2106577.

27 X. Lv, J. Li, L. Xu, X. Zhu, A. Tameev, A. Nekrasov, G. Kim, H. Xu and C. Zhang, *ACS Appl. Mater. Interfaces*, 2021, **13**, 41826–41835.

28 M. Shao, D. Ji, Z. Xu, J. Dong, X. Lv, M. Ouyang, Y. Lv, D. S. Wright and C. Zhang, *J. Power Sources*, 2023, **581**, 233490.

29 G. Yang, Y. M. Zhang, Y. Cai, B. Yang, C. Gu and S. X. Zhang, *Chem. Soc. Rev.*, 2020, **49**, 8687–8720.

30 B. Wang, W. Zhang, F. Zhao, W. W. Yu, A. Y. Elezzabi, L. Liu and H. Li, *Nano Mater. Sci.*, 2022, **5**, 369–391.

31 W. Zhang, H. Li, E. Hopmann and A. Y. Elezzabi, *Nanophotonics*, 2020, **10**, 825–850.

32 S. Zhang, Y. Li, T. Zhang, S. Cao, Q. Yao, H. Lin, H. Ye, A. Fisher and J. Y. Lee, *ACS Appl. Mater. Interfaces*, 2019, **11**, 48062–48070.

33 S. Huang, R. Zhang, P. Shao, Y. Zhang and R. T. Wen, *Adv. Opt. Mater.*, 2022, **10**, 2200903.

34 J. Wang, W. Zhao, B. Tam, H. Zhang, Y. Zhou, L. Yong and W. Cheng, *Chem. Eng. J.*, 2023, **452**, 139655.

35 W. Zhao, J. Wang, B. Tam, P. Pei, F. Li, A. Xie and W. Cheng, *ACS Appl. Mater. Interfaces*, 2022, **14**, 30021–30028.

36 J. Kim, G. K. Ong, Y. Wang, G. LeBlanc, T. E. Williams, T. M. Mattox, B. A. Helms and D. J. Milliron, *Nano Lett.*, 2015, **15**, 5574–5579.

37 B. Huang, J. Song, J. Zhong, H. Wang, X. Zheng, J. Jia, S. Yun, D. You, H. Kimura and L. Kang, *Chem. Eng. J.*, 2022, **449**, 137850.

38 H. Li, W. Zhang and A. Y. Elezzabi, *Adv. Mater.*, 2020, **32**, 2003574.

39 Q. Meng, S. Cao, J. Guo, Q. Wang, K. Wang, T. Yang, R. Zeng, J. Zhao and B. Zou, *J. Energy Chem.*, 2022, **77**, 137–143.

40 Y. Yao, Q. Zhao, W. Wei, Z. Chen, Y. Zhu, P. Zhang, Z. Zhang and Y. Gao, *Nano Energy*, 2020, **68**, 104350.

41 S. Cao, S. Zhang, T. Zhang, Q. Yao and J. Y. Lee, *Joule*, 2019, **3**, 1152–1162.

42 Y. Liang, S. Cao, Q. Wei, R. Zeng, J. Zhao, H. Li, W. W. Yu and B. Zou, *Nano-Micro Lett.*, 2021, **13**, 196.

43 S. Zhang, S. Cao, T. Zhang and J. Y. Lee, *Adv. Mater.*, 2020, **32**, 2004686.

44 S. Zhang, S. Cao, T. Zhang, Q. Yao, A. Fisher and J. Y. Lee, *Mater. Horiz.*, 2018, **5**, 291–297.

45 S. Zhang, S. Cao, T. Zhang, A. Fisher and J. Y. Lee, *Energy Environ. Sci.*, 2018, **11**, 2884–2892.

46 H. Li, L. McRae, C. J. Firby and A. Y. Elezzabi, *Adv. Mater.*, 2019, **31**, 1807065.

47 Q. Zhao, J. Wang, X. Ai, Z. Pan, F. Xu, J. Wang and Y. Gao, *Nano Energy*, 2021, **89**, 106356.

48 Q. Meng, S. Cao, J. Guo, Q. Wang, K. Wang, T. Yang, R. Zeng, J. Zhao and B. Zou, *J. Energy Chem.*, 2023, 77, 137–143.

49 S. Cong, Y. Tian, Q. Li, Z. Zhao and F. Geng, *Adv. Mater.*, 2014, **26**, 4260–4267.

50 Y. Yao, Q. Zhao, W. Wei, Z. Chen, Y. Zhu, P. Zhang, Z. Zhang and Y. Gao, *Nano Energy*, 2020, **68**, 104350.

51 D. McManus, S. Vranic, F. Withers, V. Sanchez-Romaguera, M. Macucci, H. Yang, R. Sorrentino, K. Parvez, S. K. Son, G. Iannaccone, K. Kostarelos, G. Fiori and C. Casiraghi, *Nat. Nanotechnol.*, 2017, **12**, 343–350.

52 G. Li, Z. Meng, J. Qian, C.-L. Ho, S. P. Lau, W.-Y. Wong and F. Yan, *Mater. Today Energy*, 2019, **12**, 155–160.

53 P. Yang, L. Zhang, D. J. Kang, R. Strahl and T. Kraus, *Adv. Opt. Mater.*, 2019, **8**, 1901429.

54 G. Hu, J. Kang, L. W. T. Ng, X. Zhu, R. C. T. Howe, C. G. Jones, M. C. Hersam and T. Hasan, *Chem. Soc. Rev.*, 2018, **47**, 3265–3300.

55 L. Zhang, D. Chao, P. Yang, L. Weber, J. Li, T. Kraus and H. J. Fan, *Adv. Energy Mater.*, 2020, **10**, 2000142.

56 M. Barawi, G. Veramonti, M. Epifani, R. Giannuzzi, T. Sibillano, C. Giannini, A. Rougier and M. Manca, *J. Mater. Chem. A*, 2018, **6**, 10201–10205.

57 S. Cao, S. Zhang, T. Zhang and J. Y. Lee, *Chem. Mater.*, 2018, **30**, 4838–4846.

58 R. Giannuzzi, T. Prontera, D. M. Tobaldi, M. Pugliese, L. De Marco, S. Carallo, G. Gigli, R. C. Pullar and V. Maiorano, *Nanotechnology*, 2021, **32**, 045703.

59 L. De Trizio, R. Buonsanti, A. M. Schimpf, A. Llordes, D. R. Gamelin, R. Simonutti and D. J. Milliron, *Chem. Mater.*, 2013, **25**, 3383–3390.

60 C. J. Dahlman, Y. Tan, M. A. Marcus and D. J. Milliron, *J. Am. Chem. Soc.*, 2015, **137**, 9160–9166.

61 S. Cao, S. Zhang, T. Zhang, A. Fisher and J. Y. Lee, *J. Mater. Chem. C*, 2018, **6**, 4007–4014.

62 A. Agrawal, S. H. Cho, O. Zandi, S. Ghosh, R. W. Johns and D. J. Milliron, *Chem. Rev.*, 2018, **118**, 3121–3207.

63 T. R. Gordon, M. Cargnello, T. Paik, F. Mangolini, R. T. Weber, P. Fornasiero and C. B. Murray, *J. Am. Chem. Soc.*, 2012, **134**, 6751–6761.

64 S. Zhang, S. Cao, T. Zhang and J. Y. Lee, *Adv. Mater.*, 2020, **32**, 2004686.

65 P. Lei, J. Wang, P. Zhang, S. Liu, S. Zhang, Y. Gao, J. Tu and G. Cai, *J. Mater. Chem. C*, 2021, **9**, 14378–14387.

66 X. Ju, F. Yang, X. Zhu and X. Jia, *ACS Sustainable Chem. Eng.*, 2020, **8**, 12222–12229.

67 J. Wang, R. Zhu, Y. Gao, Y. Jia and G. Cai, *J. Phys. Chem. Lett.*, 2023, **14**, 2284–2291.

68 K. J. Griffith, K. M. Wiaderek, G. Cibin, L. E. Marbella and C. P. Grey, *Nature*, 2018, **559**, 556–563.

69 R. Ren, S. Liu, Y. Gao, P. Lei, J. Wang, X. Tong, P. Zhang, Z. Wang and G. Cai, *ACS Energy Lett.*, 2023, **8**, 2300–2307.

70 H. Liu, Y. Zhang, P. Lei, J. Feng, S. Jia, J. Huang, C. Hu, C. Bian and G. Cai, *ACS Appl. Mater. Interfaces*, 2023, **15**, 23412–23420.

71 Y. Huang, B. Wang, X. Bai, Y. Han, W. Zhang, C. Zhou, H. Meng, F. Chen, X. Wu, Q. Jiang, R. Li, S. Zhang, X. Jia and R. Zhang, *Adv. Opt. Mater.*, 2022, **10**, 2102399.

72 H. Li, L. McRae, C. J. Firby and A. Y. Elezzabi, *Adv. Mater.*, 2019, **31**, 1807065.

73 Q. Zhao, J. Wang, X. Ai, Z. Pan, F. Xu, J. Wang and Y. Gao, *Nano Energy*, 2021, **89**, 106356.

74 J. L. Wang, J. W. Liu, S. Z. Sheng, Z. He, J. Gao and S. H. Yu, *Nano Lett.*, 2021, **21**, 9203–9209.

75 S.-Z. Sheng, J.-L. Wang, B. Zhao, Z. He, X.-F. Feng, Q.-G. Shang, C. Chen, G. Pei, J. Zhou, J.-W. Liu and S.-H. Yu, *Nat. Commun.*, 2023, **14**, 3231.

76 W. Zhang, H. Li, W. W. Yu and A. Y. Elezzabi, *Light: Sci. Appl.*, 2020, **9**, 121.

77 B. Wang, F. Zhao, W. Zhang, C. Li, K. Hu, B. N. Carnio, L. Liu, W. W. Yu, A. Y. Elezzabi and H. Li, *Small Sci.*, 2023, **3**, 2300046.

78 L. Tang, J. Tan, H. Nong, B. Liu and H.-M. Cheng, *Acc. Mater. Res.*, 2020, **2**, 36–47.

79 A. Azam, J. Kim, J. Park, T. G. Novak, A. P. Tiwari, S. H. Song, B. Kim and S. Jeon, *Nano Lett.*, 2018, **18**, 5646–5651.

80 R. Li, X. Ma, J. Li, J. Cao, H. Gao, T. Li, X. Zhang, L. Wang, Q. Zhang, G. Wang, C. Hou, Y. Li, T. Palacios, Y. Lin, H. Wang and X. Ling, *Nat. Commun.*, 2021, **12**, 1587.

81 L. Lin, H. Peng and Z. Liu, *Nat. Mater.*, 2019, **18**, 520–524.

82 A. VahidMohammadi, J. Rosen and Y. Gogotsi, *Science*, 2021, **372**, 1165.

83 F. Lu, D. Shi, P. Tan and Y. Han, *Chem. Eng. J.*, 2022, **450**, 138324.

84 D. Pang, M. Alhabeb, X. Mu, Y. Dall'Agnese, Y. Gogotsi and Y. Gao, *Nano Lett.*, 2019, **19**, 7443–7448.